A Parabrachial to Hypothalamic Pathway Mediates Defensive Behavior

Fan Wang[1,2†], Yuge Chen[1,2†], Yuxin Lin[1,2$], Xuze Wang[1,2$], Kaiyuan Li[1,2], Yong Han[1,2], Jintao Wu[1,2], Xingyi Shi[1,2], Zhenggang Zhu[1,2], Chaoying Long[1,2], Xiaojun Hu[1,3], Shumin Duan[1,2,3,4,5,6]* and Zhihua Gao[1,2,3]*

[1]Department of Neurobiology and Department of Neurology of Second Affiliated Hospital, Zhejiang University School of Medicine, Hangzhou, P.R. China;

[2]Liangzhu Laboratory, Zhejiang University Medical Center, The MOE Frontier Science Center for Brain Research and Brain-Machine Integration, Zhejiang University School of Brain Science and Brain Medicine, Hangzhou, P.R. China.

[3]NHC and CAMS Key Laboratory of Medical Neurobiology, MOE Frontier Science Center for Brain Science and Brain-Machine Integration, School of Brain Science and Brain Medicine, Zhejiang University, Hangzhou, P.R. China;

[4]Institute for Translational Brain Research, MOE Frontiers Center for Brain Science, Fudan University, Shanghai, P.R. China;

[5]The Institute of Brain and Cognitive Sciences, Zhejiang University City College, Hangzhou, P.R. China;

[6]Chuanqi Research and Development Center of Zhejiang University, Hangzhou, P.R. China

[†]These authors contributed equally to this work

[$] These authors contributed equally to this work

*For correspondence: duanshumin@zju.edu.cn (S.D.); zhihuagao@zju.edu.cn (Z.G.)

Abstract

Defensive behaviors are critical for animal's survival. Both the paraventricular nucleus of the hypothalamus (PVN) and the parabrachial nucleus (PBN) have been shown to be involved in defensive behaviors. However, whether there are direct connections between them to mediate defensive behaviors remains unclear. Here, by retrograde and anterograde tracing, we uncover that cholecystokinin (CCK)-expressing neurons in the lateral PBN (LPB^{CCK}) directly project to the PVN. By *in vivo* fiber photometry recording, we found that LPB^{CCK} neurons actively respond to various threat stimuli. Selective photoactivation of LPB^{CCK} neurons promotes aversion and defensive behaviors. Conversely, photoinhibition of LPB^{CCK} neurons attenuates rat or looming stimuli-induced flight responses. Optogenetic activation of LPB^{CCK} axon terminals within the PVN or PVN glutamatergic neurons promote defensive behaviors. Whereas chemogenetic and pharmacological inhibition of local PVN neurons prevent LPB^{CCK}-PVN pathway activation-driven flight responses. These data suggest that LPB^{CCK} neurons recruit downstream PVN neurons to actively engage in flight responses. Our study identifies a previously unrecognized role for the LPB^{CCK}-PVN pathway in controlling defensive behaviors.

Introduction

Living in an environment full of diverse threats, animals develop a variety of defensive behaviors for survival during evolution (Anderson & Adolphs, 2014; D. C. Blanchard, G. Griebel, & R. J. Blanchard, 2001; Crawford & Masterson, 1982; Fanselow & Bolles, 1979; LeDoux, 2012; M. Yilmaz & M. Meister, 2013). From the perspective of predator and prey interactions, defensive responses are generally divided into two categories: to avoid being discovered (such as freezing or hiding behaviors) or being caught (such as escaping or attacking behaviors) (Crawford & Masterson, 1982; Fanselow & Bolles, 1979; Melis Yilmaz & Markus Meister, 2013). Which type of defensive behavior is selected depends on many factors, including the intensity and proximity of the threat, as well as the surrounding context. In general, escape is triggered when animals are faced with an imminent threat with a shelter nearby (Eilam, 2005; Lin et al., 2022; Perusini & Fanselow, 2015; L. Sun, R. Liu, F. Guo, M. Q. Wen, X. L. Ma, et al., 2020; B. Zhang et al., 2018).

Several brain regions, including the periaqueductal gray (PAG), amygdala and medial hypothalamic zone (MHZ), have been implicated in mediating escape behaviors (Evans et al., 2018; Shang et al., 2018; Shang et al., 2015; Silva et al., 2013; Tovote et al., 2016; Wang et al., 2015; Wang, Schuette, Nagai, et al., 2021; Wei et al., 2015). Recent studies have highlighted a role for the hypothalamus, in particular the MHZ, including the anterior hypothalamic nucleus (AHN), the dorsomedial part of ventromedial hypothalamic nucleus (VMHdm) and the dorsal pre-mammillary nucleus (PMd), in mediating escape behaviors. For example, a subset of VMH neurons

63 collaterally project to the AHN and PAG to promote both escape and avoidance
64 behaviors (Wang, Chen, & Lin, 2015). Moreover, PMd neurons project to the
65 dorsolateral periaqueductal gray region (dlPAG) and the anteromedial ventral thalamic
66 region (AMV) also control escape behaviors (W. Wang, P. J. Schuette, J. Nagai, et al.,
67 2021). In addition, PVN, an area enriched with endocrine neurons, has also been
68 associated with escape behaviors. Optogenetic activation of $Sim1^{+}$ neurons in the PVN
69 triggers escape (Mangieri et al., 2019b) and projections from the PVN to both the
70 ventral midbrain region (vMB) and the ventral lateral septum (LSv) mediate defensive-
71 like behaviors, including hiding, escape jumping and hyperlocomotion (Mangieri et al.,
72 2019b; Xu et al., 2019). Despite a growing number of studies illustrating the importance
73 of PVN in mediating defensive behaviors, upstream inputs that transmit the danger
74 signals to the PVN remain unclear (Isosaka et al., 2015; Penzo et al., 2015).

75 Located in the dorsolateral pons, PBN, serves as an important relay station for
76 sensory transmission (C. E. Fulwiler & C. B. Saper, 1984). While PBN is best known
77 for various sensory processes to protect the body from noxious stimuli, emerging
78 evidence suggests that it may act as a key node in mediating defensive behaviors
79 (Campos, Bowen, Roman, & Palmiter, 2018; H. E. Day, C. V. Masini, & S. Campeau,
80 2004; Han, Mao, & Dally, 2015). Electrical lesions of the PBN or local microinjections
81 of kainic acid into the PBN induced defensive behaviors (Mileikovskii & Verevkina,
82 1991). In addition, exposure of the olfactory predator cue, trimethylthiazoline (TMT),
83 increased c-fos expression in the LPB (H. E. Day et al., 2004). More importantly,
84 calcitonin gene-related peptide (CGRP) neurons, located in the external lateral

subnuclei of PBN (PBel), have been shown to mediate alarm responses and defensive behaviors under stressful or threatening circumstances via projections to the amygdala and the bed nucleus of stria terminalis (BNST) (Song Han et al., 2015; L. Zhang, Hernández, & Eiden, 2020). While both PBN and PVN neurons appear to be involved in defensive responses, it remains unclear whether they connect with each other to mediate defensive behaviors (Carl E Fulwiler & Clifford B Saper, 1984).

Both CCK and CCK receptor-expressing neurons have been implicated in defensive behaviors (Bertoglio, de Bortoli, & Zangrossi, 2007; Chen et al., 2022; W. Wang, P. J. Schuette, M. Q. La-Vu, et al., 2021). PVN neurons also express CCK receptors and are involved in defensive behaviors (Mangieri et al., 2019a; O'Shea & Gundlach, 1993; Xu et al., 2019), raising a possibility that upstream CCK inputs to the PVN (Meister, Broberger, Villar, & Hökfelt, 1994) may be implicated in defensive behaviors. In an attempt to test this possibility, we injected the Cre-dependent retrograde tracer (AAV2-Retro-DIO-EYFP) into the PVN of CCK-Cre mice and found that the LPB is an important upstream CCKergic input to the PVN. We further showed that LPB^{CCK} neurons were recruited upon exposure to various threat stimuli. Optogenetic activation of either LPB^{CCK} neuronal somas or their projections to the PVN promotes defensive responses, whereas their inhibition attenuates defensive-like behaviors, suggesting an essential and sufficient role for LPB^{CCK}-PVN pathway in mediating defensive behaviors.

106 **Results**

107 **LPB^{CCK} neurons provide monosynaptic glutamatergic projections to the PVN**

108 To identify upstream CCKergic inputs to the PVN and visualize the range of viral
109 infection, we injected a mixture of retrograde viral tracer (AAV2-Retro-DIO-EYFP,
110 hereafter referred to as AAV2-Retro) and CTB 555 into the PVN of knock-in mice
111 expressing Cre recombinase at the CCK Locus (CCK-ires-Cre, referred to as CCK-Cre
112 hereafter) **(Figure 1A)**. We observed abundant EYFP^{+} neurons in the LPB, medial
113 orbital cortex (MO), and cingulate cortex (CC), with scattered EYFP^{+} cells in the PAG
114 and dysgranular insular cortex (DI) **(Figure 1B-H).** Since LPB is a region critical for
115 sensory signal processing, we mainly focused on the LPB in the following study
116 (Fulwiler, C.E., and Saper, C.B.,1985; Garfield AS et al., 2014).

117 LPB contains several subregions with diverse peptide-expressing neuronal
118 subtypes and CCK^{+} neurons have been shown to primarily locate within the superior
119 lateral PB (PBsl) (Garfield et al., 2014). To dissect the identity of CCK^{+} neurons in the
120 LPB, we performed *in situ* hybridization in CCK-Cre::Ai14 mice using probes for
121 *Vglut2* and *Vgat*, markers specific to glutamatergic and GABAergic neurons
122 **(Supplementary Figure 1A-C)**. We found that LPB^{CCK} neurons (84.0% ± 1.7%)
123 predominantly expressed *Vglut2*, with a tiny subpopulation (2.0% ± 1.2%) expressed
124 expressing *Vgat*, suggesting that LPB^{CCK} neurons were mostly glutamatergic neurons
125 **(Supplementary Figure 1D-E)**. In addition, co-labeling with another neuropeptide,
126 CGRP, revealed minimal co-localization (2.2% ± 0.37%) between CCK and CGRP
127 **(Supplementary Figure 1F-G)**, suggesting primary separation between these two

128 subpopulations of neurons. Collectively, these data demonstrate that LPB^{CCK} neurons
129 comprise predominantly glutamatergic neurons, which barely overlap with CGRP
130 neurons.

131 To verify the anatomical connections between the LPB and PVN, we injected the
132 anterograde viral tracer (AAV-hSyn-FLEx-mGFP-2A-Synaptophysin-mRuby) into the
133 LPB of CCK-Cre mice **(Figure 1I-J)**. We observed prominent GFP^+ fibers and $mRuby^+$
134 bouton-like structures, reminiscent of axonal terminals, within the PVN **(Figure 1K)**
135 and other brain regions **(Supplementary Figure 2A-L).** Next, we injected the Cre-
136 dependent adeno-associated virus (AAV) expressing channelrhodopsin-2 virus
137 (AAV2/9-DIO-ChR2-EYFP) into the LPB of CCK-Cre mice **(Figure 1L)** and
138 optogenetically stimulated the axonal terminals of virus-labeled LPB^{CCK} neurons within
139 the PVN in brain slices. We successfully recorded light stimulation-induced excitatory
140 postsynaptic currents (EPSCs), rather than inhibitory postsynaptic currents (IPSCs).
141 These EPSCs were blocked in the presence of the sodium channel antagonist
142 tetrodotoxin (TTX), but rescued by the potassium channel antagonist 4-Aminopyridine
143 (4-AP) **(Figure 1M-N)**. Further, NMDA receptor antagonist AP5, and AMPA receptor
144 antagonist CNQX also blocked light stimulation-induced EPSCs **(Figure 1O-P)**,
145 validating that PVN neurons receive monosynaptic excitatory innervations from
146 LPB^{CCK} neurons.

147

148 **Photostimulation of LPB^{CCK} neurons induces aversion and defensive behaviors**

149 LPB^{CCK} neurons have been shown to regulate glucose homeostasis and body

150 temperature (Garfield et al., 2014; W. Z. Yang, Du, Zhang, Gao, & Shen, 2020).
151 However, it remains unclear whether activation of LPB^{CCK} neurons may elicit direct
152 behavioral changes. Before optic stimulation *in vivo*, we first tested the efficacy of
153 optogenetic stimulation by whole-cell recording in ChR2-expressing LPB^{CCK} neurons.
154 We observed that 5-20 Hz blue laser pulses induced time-locked action potential firing,
155 with 20 Hz inducing maximal firing capacities. We then chose 20 Hz for the following
156 *in vivo* stimulation **(Figure 2 A).**

157 We injected the control or ChR2-expressing viruses (AAV2/9-EF1a-DIO-EYFP or
158 AAV2/9-EF1a-DIO-ChR2-EYFP) into the LPB of CCK-Cre mice, followed by optical
159 fiber implantation and optic stimulation **(Figure 2B-D).** Since LPB has been shown to
160 mediate aversion (Chiang et al., 2019; Li et al., 2020), we first tested whether
161 optogenetic activation of LPB^{CCK} neurons affects aversion using the real-time place
162 aversion (RTPA) test **(Figure 2E).** We found that activation of LPB^{CCK} neurons
163 significantly reduced the duration of mice in the laser-paired chamber, accompanied by
164 rapid running or flight to the other laser-unpaired chamber, indicating an obvious
165 aversion-like avoidance and/or fear-related defensive-like behaviors **(Figure 2F-G)**.

166 To further investigate whether LPB^{CCK} neurons plays a role in defensive behaviors,
167 we used a well-established flight-to-nest behavioral test by putting a nest in the corner
168 of an arena to test the ability of mice to actively search for hiding **(Figure 2H)**. Of note,
169 activating LPB^{CCK} neurons induced robust flight-to-nest behavior in mice, with much
170 shorter latency and faster speed running towards the nest (latency: EYFP, 87.71 ± 22.38
171 s vs. ChR2, 7.571 ± 0.8123 s; speed: EYFP, 184.4% ± 30.4% vs. ChR2, 361.7% ±

172 31.5%), followed by longer stay in the nest (EYFP, 63.906% ± 3.645% vs. ChR2, 97.26%
173 ± 2.737%) **(Figure 2I-K)**. These data suggest that activation of LPB^{CCK} neurons
174 induces aversion-like avoidance and defensive-like flight-to-nest behaviors.

175 Defensive behaviors are usually accompanied by changes in the autonomic
176 nervous system, such as increased heart rates, dilated pupil size and elevated cortisol
177 levels (Dong et al., 2019; Gross & Canteras, 2012; Wang et al., 2015). We found that
178 photostimulation of LPB^{CCK} neurons also significantly increased heart rates and
179 enlarged pupil diameters, along with elevated plasma levels of corticosterone **(Figure**
180 **2L-P)**, suggesting that activating LPB^{CCK} neurons induces fast sympathetic changes,
181 leading to an arousal state accompanying the defensive responses in mice (Salay, Ishiko,
182 & Huberman, 2018).

183 Since activation of LPB^{CCK} neurons induced fear-associated flight-to-nest
184 behaviors and long-term fear may trigger anxiety-like states in animals (Tovote et al.,
185 2005; H. Yang et al., 2016), we also examined whether prolonged activation of LPB^{CCK}
186 neurons induces anxiety-like behaviors **(Supplementary 3A)**. After 10 min of light
187 stimulation, mice injected with ChR2 exhibited significantly reduced, center time and
188 center entries in the open field tests without affecting total distance, and decreased open
189 arm entries and time in the elevated plus maze tests **(Supplementary 3B-J)**, suggesting
190 that prolonged activation of LPB^{CCK} neurons also induces anxiety-like behaviors in
191 mice.

192

193 **LPB^{CCK} neurons encode threat stimuli-evoked flight behaviors**

194 LPB neurons were shown to be activated when animals are in proximity to dangerous

stimuli (Campos et al., 2018; Heidi EW Day, Cher V Masini, & Serge Campeau, 2004; Sung Han, Matthew T. Soleiman, Marta E. Soden, Larry S. Zweifel, & Richard D. Palmiter, 2015). To track the endogenous activities of LPB^{CCK} neurons *in vivo*, we injected the Cre-dependent fluorescent calcium indicator AAV-DIO-GCaMP7s into the LPB of CCK-Cre mice, and recorded the calcium responses by fiber photometry **(Figure 3A-C)**. Consistent with previous observation (W. Z. Yang et al., 2020), we observed elevated calcium responses of LPB^{CCK} neurons by heat stimuli (43°C) **(Supplementary Figure 4A-D)**. We then tested the response of these neurons in a predator-exposure assay, in which an awake but restrained rat was placed at one end of a rectangular arena (Reis et al., 2021; Weisheng Wang et al., 2021), and a mouse was placed at the other end, away from the rat. After perceiving the presence of the rat, mice usually exhibit risk assessment behaviors by curiously approaching and investigating the rat (Olivier, Mos, & Slangen, 1991). We observed that the calcium signals of LPB^{CCK} neurons gradually rise when mice approached the rat. At the moment of escape initiation, when mice turned back and dashed away from the rat, the calcium signals reached a peak **(Figure 3D-G, 3L)**. However, the signals ramped down as mice gained distance from the rat**.** Notably, activities of LPB^{CCK} neurons were unaffected in the presence of a toy rat (**Supplementary Figure 4E-H**).

In the presence of the visual predatory cue, such as appearing and expanding looming shadows to mimic an approaching predator (Melis Yilmaz & Markus Meister, 2013), LPB^{CCK} neurons also showed increased calcium signals (Figures 3H). Similar to rat exposure assay, we also tested the response of these neurons in the looming assay,

217 the elevated calcium signals reached peak when the animal initiated escape, but reduced
218 once it ran into the nest (**Figure 3H-K, 3M**). LPB^{CCK} neurons also showed elevated
219 calcium signals when mice were exposed to the olfactory predatory cue, TMT odor
220 (**Supplementary Figure 4I-L**). Correlative analysis revealed that the elevation of the
221 calcium signal was correlated with the onset of escape responses (**Figure 3N-O**). Thus,
222 threatening stimuli of different sensory predatory cue stimulated the LPB^{CCK} neurons
223 (**Figure 3P-R**). Together, these data demonstrate that LPB^{CCK} neurons encode innate
224 threat stimuli-evoked aversion and flight behaviors.
225

226 **Inhibition of LPB^{CCK} neurons suppressed predatory cue-evoked flight responses**

227 To examine whether LPB^{CCK} neurons are required for innate threat-evoked defensive
228 behaviors, we then inhibited LPB^{CCK} neurons using optogenetic tools. By injecting the
229 Cre-dependent AAV expressing the guillardia theta anion channel rhodopsins-1
230 (GtACR1) into the LPB of CCK-Cre mice, followed by optic stimulation, we were able
231 to effectively inhibit the firing of LPB^{CCK} neurons **(Figure 4A)**. Next, we bilaterally
232 injected the control or GtACR1 viruses into the LPB and photo-inhibited these neurons
233 *in vivo* **(Figure 4B-C).** In the rat exposure test **(Figure 4D-E)**, after a quick exploration
234 of the rat in the corner (the danger zone), control mice usually fled to the other end of
235 the box (the putative safe zone). However, optic inhibition of LPB^{CCK} neurons
236 significantly increased the time (EYFP, 7.247% ± 2.329% vs. GtACR1, 26.57% ±
237 5.375%) and entries (EYFP, 6.167 ± 1.579 vs. GtACR1, 12.67 ± 2.141) of mice to the
238 danger zone, with no effect on total travel distance (EYFP, 8.837 ± 1.934 m vs. GtACR1,

12.69 ± 1.421 m), suggesting a delayed flight response **(Figure 4F-H)**. In the looming test **(Figure 4I-J)**, inhibition of LPB^{CCK} neurons also increased the latency fleeing to the nest (EYFP, 10.18 ± 2.828 s vs. GtACR1, 27.14 ± 6.526 s), followed by reduced hiding time in the nest (EYFP, 85.36% ± 9.846% vs. GtACR1, 39.17% ± 16.36%) **(Figure 4K-L)**. Our data suggest that LPB^{CCK} neurons are required for proper defensive behaviors to rat exposure and looming stimuli.

Stimulation of the LPB^{CCK}-PVN pathway triggers defensive-like flight-to-nest behaviors

To further investigate whether activation of the LPB^{CCK}-PVN pathway induces defensive-like flight-to-nest behavior, we unilaterally injected the control or ChR2 virus into the LPB of CCK-Cre mice and implanted an optical fiber above the PVN **(Figure 5A-E)**. By photostimulating the axonal terminals of LPB^{CCK} neurons within the PVN, we also observed shorter latency (EYFP, 73.43 ± 21.08 s vs. ChR2, 8 ± 1.047 s), faster speed (EYFP, 122.3% ± 17.81% vs. ChR2, 277.9% ± 32.85%) running towards the nest, and longer stay in the nest; (EYFP, 3.751% ± 1.23% vs. ChR2, 89.29% ± 10.71%) **(Figure 5F-H)**, similar to soma activation. Post-hoc c-fos staining further verified the activation of PVN neurons after optic stimulation **(Figure 5I-J)**. As well, terminal activation also increased heart rates **(Figure 5K)** and plasma corticosterone levels **(Figure 5N)**, but with no effects on pupil size **(Figure 5L-M)**. Together, these data suggest that activation of the LPB^{CCK}-PVN pathway is sufficient to trigger flight-to-nest behavior, along with increased heart rates and corticosterone levels.

261

262 **PVN is required for defensive responses to threatening situations**

263 Since LPB^{CCK} neurons project to multiple regions **(Supplementary Figure 2A-I)**, the
264 effects observed upon their activation may arise from different downstream targets,
265 other than the PVN. To test this possibility, we investigated whether inhibition of the
266 PVN is required for the LPB^{CCK} neurons-induced defensive-like flight-to-nest behavior.
267 To achieve this aim, we used a dual virus-mediated optogenetic activation and
268 chemogenetic inhibition strategy, by injecting AAV2/9-DIO-ChR2-EYFP into the LPB,
269 and AAV2/9-hsyn-hM4Di-mCherry into the PVN of CCK-Cre mice. By putting an
270 optical fiber above the PVN, we were able to activate the LPB^{CCK} terminals and induce
271 defensive-like flight-to-nest behavior as shown above **(Figure 6A-B)**. Upon CNO
272 administration to inhibit PVN neurons, we observed a much longer latency, lower speed
273 of the mice in returning to the nest, and reduced hiding time in the nest (latency: saline,
274 8.286 ± 1.475 s vs. CNO, 18.29 ± 2.843 s; speed: saline, 289.3% ± 25.22% vs. CNO,
275 124.7% ± 13.67%; time in the nest: saline, 81.55% ± 11.16% vs. CNO, 25.83% ±
276 10.32%) **(Figure 6C-E)**. These data suggest that the PVN is a required downstream
277 target for LPB^{CCK} neurons activation-induced defensive behavior.

278 LPB^{CCK} neurons may release either glutamate or neuropeptide CCK to induce the
279 defensive behavior. To determine which neurotransmitter or modulator is engaged in
280 the above responses, we combined pharmacologic with optogenetic manipulation. Two
281 types of CCK receptors are present in the central nervous system and CCKaR is widely
282 distributed throughout the PVN, whereas the expression of CCKbR in PVN is low

283 **(Supplementary Figure 5A-B)**. We infused glutamate receptor antagonists (CNQX +
284 AP5), CCK receptor antagonists (Devazepide + L-365,260), or artificial cerebrospinal
285 fluid (aCSF) through an implanted cannula 30-min before optogenetic activation of
286 LPB^{CCK} neurons **(Figure 6F-H)**. We found that blocking glutamate receptors induced
287 a longer latency, slower speed in returning to the nest, along with reduced hiding time
288 in the nest **(Figure 6I-K)**, when compared with aCSF-treated mice. However, blocking
289 CCK receptors showed no significant effects **(Figure 6I-K).** These results suggest that
290 glutamatergic transmission from LPB^{CCK} neurons to the PVN mediates defensive-like
291 flight-to-nest behavior.
292

293 **Photostimulation of PVN^{Vglut2} neurons promotes defensive-like flight-to-nest**
294 **behavior**

295 Of note, PVN neurons are mostly glutamatergic (Vong et al., 2011; Xu et al., 2013). We
296 further assessed whether optogenetic activation of PVN^{Vglut2} neurons elicit defensive-
297 like behavior **(Figure 6L-M)**. We found that optogenetic activation of PVN^{Vglut2}
298 neurons also induced flight-to-nest behavior (latency: EYFP, 127.5 ± 22.5 s vs. ChR2,
299 12.83 ± 2.937 s; speed: EYFP, 142.4 ± 32.07% vs. ChR2, 384.4% ± 83.52%), followed
300 by longer hiding time in the nest (EYFP, 0.2783% ± 0.2783% vs. ChR2, 61.11% ±
301 17.58%) **(Figure 6N-P)**, compared to the control. These data suggest that optogenetic
302 activation of PVN^{Vglut2} neurons was sufficient to evoke defensive-like flight-to-nest
303 behavior.

304 PVN^{CRH} neurons have recently been shown to predict the occurrence of defensive

behaviors in mice (N. Daviu et al., 2020). Interestingly, optogenetic activation of the LPB^{CCK}-PVN pathway primarily activated PVN^{CRH} neurons, rather than vasopressin or oxytocin neurons **(Supplementary Figure 5C-F).** However, optogenetic activation of PVN^{CRH} neurons was not sufficient to drive defensive-like flight-to-nest behavior **(Supplementary 5G-K)** (latency: EYFP, 77 ± 20.69 s vs. ChR2, 90.17 ± 22.03 s; speed: EYFP, 156.6 ± 22.59% vs. ChR2, 217.2% ± 61.54%; time in the nest: EYFP, 20.95% ± 13.89% vs. ChR2, 35.28% ± 20.48%).

327 **Discussion**

328 Defensive behaviors are actions that are naturally selected to avoid or reduce potential
329 harm for the survival of animal species. While emerging evidence has suggested that
330 LPB are associated with sensation of danger signals and aversive stimuli (Campos et
331 al., 2018; Heidi EW Day et al., 2004; Sung Han et al., 2015), we found that LPB^{CCK}
332 neurons are actively recruited upon exposure to various predatory stimuli. Activating
333 LPB^{CCK} neurons triggers aversive-like avoidance and defensive-like flight responses,
334 whereas inhibition of these neurons suppressed predatory stimuli-induced defensive
335 behaviors. Inhibition of downstream PVN neurons attenuated photoactivation of
336 LPB^{CCK}-PVN terminals-promoted flight responses, suggesting that LPB^{CCK}-PVN
337 pathway is important for the regulation of defensive responses. Our study thus reveals
338 a new connection from the brainstem to the hypothalamus to regulate innate defensive
339 behaviors **(Figure 6Q)**.

340 Hippocampal and cortical CCK-expressing neurons have been thought of mainly
341 GABAergic (X. Liu, Dimidschstein, Fishell, & Carter, 2020; X. C. Sun et al., 2020;
342 Whissell, Cajanding, Fogel, & Kim, 2015). We found that LPB^{CCK} neurons are
343 predominantly glutamatergic, similar to those in the amygdala (Shen et al., 2019).
344 While the roles of LPB^{CGRP} neurons have been associated with the passive defensive
345 responses (S. Han, M. T. Soleiman, M. E. Soden, L. S. Zweifel, & R. D. Palmiter, 2015;
346 Keay & Bandler, 2001), we show that activation of LPB^{CCK} neurons primarily triggers
347 active defensive responses, such as flight-to-nest behaviors (Keay & Bandler, 2001).
348 The fact that CGRP and CCK neurons are spatially segregated, responsive to distinct

threat signals and involved in different defensive responses, indicating that LPB acts as an important integration center or hub to gate defensive responses when animals encounter different threats (S. Liu et al., 2022; Tokita, Inoue, & Boughter Jr, 2009). It would be interesting to investigate whether LPB^{CCK} and LPB^{CGRP} neurons coordinately regulate defensive responses under different threatening situations.

In vivo calcium imaging showed that LPB^{CCK} neurons increase firing upon exposure to predators and/or predatory cues, which occurs before the initiation of an escape behavior. These findings indicate that LPB^{CCK} neurons may produce a preparatory signal before the escape initiation, which allows the downstream targets to further assess the threat signals, plan escape routes and take appropriate motor actions. LPB^{CCK} neurons are well positioned to play such an important role in linking the imminent threat to escape initiation, as they receive inputs from both the peripheral and visceral sensory system and project to many brain regions involved in defensive responses including the hypothalamus, PVT and PAG (Cooper Jr & Blumstein, 2015; Ellard & Eller, 2009; Song Han et al., 2015; Krout & Loewy, 2000; Saper & Loewy, 1980; Sun, Liu, Guo, Wen, & Duan, 2020; Tokita et al., 2009). While PVN^{CRH} or PAG^{CCK} neurons have also been shown to be recruited during flight, their peak activity did not match the flight initiation, but occurred during flight (Núria Daviu et al., 2020; La-Vu et al., 2022). The peak activities of LPB^{CCK} neurons at the onset of escape suggest that LPB^{CCK} neurons likely gate and instruct the escape rather than directly control locomotive behaviors.

Despite many early studies mapping downstream projections for LPB neurons (S.

371 Han et al., 2015; Saper & Loewy, 1980; L. Sun, R. Liu, F. Guo, M. Q. Wen, X. L. Ma,
372 et al., 2020), we are the first to demonstrate that LPB^{CCK} neurons directly connect with
373 PVN neurons. Direct projections from the brainstem to the hypothalamus for the escape
374 responses may be more conducive to escape in emergency situations. Besides the PVN,
375 we also observed that LPB^{CCK} neurons project to the PVT, VMH and PAG, which have
376 also been associated with aversion and/or defensive behaviors (LeDoux, 2012; Vianna,
377 Landeira-Fernandez, & Brandão, 2001; Wang et al., 2015). It would be interesting to
378 further investigate how these different downstream areas coordinately contribute to
379 defensive responses.

380 PVN is important for neuroendocrine and autonomous regulation (Canteras,
381 Ribeiro-Barbosa, & Comoli, 2001; Coote, 2005; Ferguson, Latchford, & Samson, 2008;
382 Sutton, Myers, & Olson, 2016). While earlier c-fos staining analyses suggest that PVN
383 neurons are activated in response to different threat stimuli (Canteras et al., 2001; Faturi,
384 Rangel, Baldo, & Canteras, 2014; Martinez, Carvalho-Netto, Amaral, Nunes-de-Souza,
385 & Canteras, 2008; Staples, McGregor, Apfelbach, & Hunt, 2008), it remains unclear
386 whether they are only involved in neuroendocrine responses or also defensive behaviors.
387 Increasing evidence has demonstrated that PVN neurons play important roles in
388 defensive behaviors independent of hormonal actions (N. Daviu et al., 2020; Mangieri
389 et al., 2019b; Xu et al., 2019). Sim1, as a specific marker of PVN, studies have reported
390 that photoactivation of PVN^{Sim1} neurons induced defensive responses (Mangieri et al.,
391 2019b). Our findings support a role for PVN neurons in mediating behavioral responses,
392 as photoactivation of PVN^{Vglut2} neurons promoted flight-to-nest behavior. Intriguingly,

stimulating the LPB^{CCK}-PVN pathway promoted flight-to-nest behaviors but activating of PVN^{CRH} neurons did not induce apparent flight-to-nest behaviors. Since PVN^{CRH} neurons receive multiple inputs and activation of the PVN^{CRH} neurons have been shown to induce aversion (Kim et al., 2019), future studies using input-specific activation of PVN^{CRH} neuronal subpopulations would further dissect the role of LPB^{CCK}- PVN^{CRH} pathway in defensive responses. Future studies using additional projection-specific approaches and more genetically defined cell tools may help resolve this problem.

Our data show that activation of LPB^{CCK} neurons drives defensive and anxiety-like behaviors, evoking an arousal and stressed states. Fear, anxiety and stress responses are closely associated with mental illnesses with dysregulated neural circuits (D Caroline Blanchard, Guy Griebel, & Robert J Blanchard, 2001). It is worth further investigation to examine whether alterations of the LPB^{CCK}-PVN pathway are implicated in these diseases and whether manipulation of this pathway might be an effective strategy for therapeutic targeting.

407 **Materials and Methods**

408 **Key resources table**

409

Reagent type (species) or resource	Designation	Source or reference	Identifiers	Additional information
Strain, strain background (Mus musculus)	CCK-ires-Cre(Cck$^{tm1.1(cre)Zjh}$/J)	The Jackson Laboratory	JAX012706	
Strain, strain background (Mus musculus)	CRH-ires-Cre (B6(Cg)-Crh$^{tm1(cre)Zjh}$/J	The Jackson Laboratory	JAX012704	
Strain, strain background (Mus musculus)	Vglut2-ires-Cre (Slc17a6$^{tm2(cre)Lowl}$/J)	The Jackson Laboratory	JAX 016963	
Strain, strain background (Mus musculus)	Ai14 (B6;129S6-Gt(ROSA)26Sor$^{tm14(CAG-tdTomato)Hze}$/J)	The Jackson Laboratory	JAX007908	
Strain, strain background (Mus musculus)	Ai3; (B6.Cg-Gt (ROSA)26Sor$^{tm3(CAG-EYFP)Hze}$/J)	The Jackson Laboratory	JAX007903	
Strain, strain background (Mus musculus)	C57BL6/J	Shanghai SLAC Laboratory Animal Co. Ltd	http://www.slaccas.com/	
Antibody	Anti-Dsred, rabbit polyclonal	Takara	Cat# 632496 RRID: AB_10013483	(1:800)
Antibody	Anti-CGRP, mouse monoclonal	Abcam	Cat# 81887 RRID: AB_1658411	(1:800)
Antibody	Anti-GFP, goat polyclonal	Abcam	Cat# 5450 RRID: AB_304896	(1:500)
Antibody	Anti-CRH, rabbit polyclona	Phoenix Biotech	Cat# H-019-06	(1:500)
Antibody	Anti-c-fos, Guinea pig polyclonal	Synaptic Systems	Cat# 226004 RRID: AB_2619946	(1:10000)
Antibody	Alexa Fluor 488 donkey anti-guinea pig IgG (H+L)	Jackson	Cat#112-486-068 RRID: AB_2617153	(1:1000)
Antibody	Alexa Fluor 555 donkey anti-rabbit IgG (H+L)	Invitrogen	Cat#A31572 RRID: AB_162543	(1:1000)
Antibody	Alexa Fluor 488 donkey anti-mouse	Invitrogen	Cat# R37114 RRID: AB_2556542	(1:1000)

	IgG (H+L)			
Antibody	Alexa Fluor 488 donkey anti-goat IgG (H+L)	Invitrogen	Cat# A11055 RRID: AB_2534102	(1:1000)
Antibody	Alexa Fluor 488 donkey anti-rabbit IgG (H+L)	Jackson	Cat# R37118 RRID: AB_2556546	(1:1000)
Commercial assay or kit	RNAscope Multiplex Fluorescent Reagent Kit v2	Advanced Cell Diagnostics	Cat# 323100	
Sequence-based reagent	RNAscope probe *Slc17a6*	Advanced Cell Diagnostics	accession number NM_080853.3	probe region 1986-2998
Sequence-based reagent	RNAscope probe *Slc32a1*	Advanced Cell Diagnostics	Accession number NM_009508.2	probe region 894-2037
Sequence-based reagent	RNAscope probe *CckaR*	Advanced Cell Diagnostics	accession number NM_009827.2	probe region 328-1434
Sequence-based reagent	RNAscope probe *CckbR*	Advanced Cell Diagnostics	accession number NM_007627.4	probe region 136-1164
Chemical compound, drug	CNQX disodium salt hydrate	Sigma-Aldrich	Cat#1045	
Chemical compound, drug	Devazepide	Sigma-Aldrich	Cat#2304	
Chemical compound, drug	Clozapine N-oxide	Sigma-Aldrich	Cat#C0832	
Chemical compound, drug	L-365,260	Sigma-Aldrich	Cat#143626	
Chemical compound, drug	DAPI	Sigma-Aldrich	N/A	
Chemical compound, drug	Tween-20	Sigma-Aldrich	N/A	
Strain, strain background (AAV2/9)	AAV2/9-hEF1a-DIO-hChR2(H134R)-EYFP-WPRE-pA	Shanghai Taitool Bioscience Co.	Cat# S0199-9	Viral titers: 2.95x1013 particles/ml
Strain, strain background (AAV2/9)	AAV2/9-hEF1a-DIO-EYFP-WPRE-pA	Shanghai Taitool Bioscience Co.	Cat#S0196-9	Viral titers:$1.0x10^{12}$ particles/ml
Strain, strain background	AAV2/9-CAG-DIO-hGtACR1-P2A-	Shanghai Taitool Bioscience Co.	Cat# S0311-9	Viral titers:5×10^{13} particles/ml

(AAV2/9)	EGFP-WPRE-pA			
Strain, strain background (AAV2/9)	rAAV2/9-hSyn-DIO-mGFP-2A-Synaptophysin-mRuby	Shanghai Taitool Bioscience Co.	Cat# S0250-9	Viral titers :1.55x10^{13} particles/ml
Strain, strain background (AAV2/2)	rAAV2/2-Retro-hEF1a-DIO-EYFP-WPRE-pA	Shanghai Taitool Bioscience Co.	Cat# S0196-2R	Viral titers: 2.52x10^{13} particles/ml
Strain, strain background (AAV2/9)	AAV2/9-hSyn-mCherry-WPRE-pA	Shanghai Taitool Bioscience Co.	Cat# S0238-9	Viral titers: ≥1.0x10^{13} particles/ml
Strain, strain background (AAV2/9)	AAV2/9-hSyn-hM4D(Gi)-mCherry-WPRE-pA	Shanghai Taitool Bioscience Co.	Cat# S0279-9	Viral titers: ≥1.0x10^{13} particles/ml
Software, algorithm	ANY-Maze software 5.3	Global Biotech Inc.	http://www.anymaze.co.uk/	
Software, algorithm	Image J	NIH	https://imagej.nih.gov/ij/index.html;%20 RRID:SCR_003070	
Software, algorithm	GraphPad Prism 6	GraphPad Software	https://www.graphpad.com/scientificsoftware/prism/; RRID: SCR_002798	
Software, algorithm	MatLab R2016a	MathWorks	https://www.mathworks.com/products.html; RRID:SCR_001622	

Animals

CCK-ires-Cre ($Cck^{tm1.1(cre)Zjh}$/J; Stock No. 012706), CRH-ires-Cre (B6(Cg)-$Crh^{tm1(cre)Zjh}$/J; Stock No. 012704), Vglut2-ires-Cre ($Slc17a6^{tm2(cre)Lowl}$/J; Stock No. 016963), Ai14 (B6;129S6-Gt(ROSA)26$Sor^{tm14(CAG-tdTomato)Hze}$/J; Stock No. 007908), C57BL/6 mice and SD rats were obtained from the Shanghai Laboratory Animal Center. Adult male mice and SD rats were used in our study. Mice and rats housed at 22 ± 1 °C and 55 ± 5% humidity on a 12-hr light/12-hr dark cycle (light on from 07:00 to 19:00) with food and water ad libitum. All experimental procedures were approved by the

419 Animal Advisory Committee at Zhejiang University and were performed in strict
420 accordance with the National Institutes of Health Guidelines for the Care and Use of
421 Laboratory Animals. All surgeries were performed under sodium pentobarbital
422 anesthesia, and every effort was made to minimize suffering.
423
424 **Immunohistochemistry**
425 Animals were transcardially perfused with saline and 4% PFA. Brains were post-fixed
426 overnight in 4% PFA at 4 °C, followed by immersed in 30% sucrose solution. Coronal
427 sections (40 μm) were cut by a CM1950 Microtome (Leica). Immunostaining was
428 performed as previously described (Zhang et al., 2018). The brain slices were
429 permeabilized in 0.5% Triton X-100 in Tris-buffered saline, blocked with 100 mM
430 glycine and 5% bovine serum albumin (BSA) containing 5% normal donkey serum.
431 Tissue sections were subsequently incubated with diluted primary and secondary
432 antibodies as indicated, nuclei stained with 6-diamidino2-phenylindole (DAPI), and
433 slides mounted with antifade reagents. The primary antibodies used were: Guinea pig
434 anti-c-fos (Synaptic Systems, Cat# 226004), Rabbit anti-Dsred (Takara, Cat# 632496),
435 Goat anti-GFP (Abcam, Cat# 5450), Mouse anti-CGRP (Abcam, Cat# 81887). Slides
436 were imaged with a confocal microscope (Olympus FluoView FV1200).
437
438 **RNAscope in situ hybridization**
439 We used RNAscope multiplex fluorescent reagent kit and designed probes (ACDBio
440 Inc.) to perform fluorescence in situ hybridization. Mouse brain tissue was sectioned

441 into 20 μm sections by cryostat (Leica CM 1950). Then sections were mounted on slides
442 and air-dried at room temperature. Subsequently, the sections were dehydrated in 50%
443 EtOH, 70% EtOH, and 100% EtOH for 5-10 min each time and air-dried at room
444 temperature again. Thereafter, protease digestion was performed in a 40 °C HybEZ
445 oven for 30 min pretreatment, slides were hybridized with pre-warmed probe in a 40 °C
446 HybEZ oven for 2 hours. Probes used in our paper were: *Slc17a6* probe (*VgluT2,*
447 accession number NM_080853.3, probe region 1986-2998), *Slc32a1* probe (*VGAT*,
448 accession number NM_009508.2, probe region 894-2037), *CCKaR* probe (accession
449 number NM_009827.2, probe region 328-1434), *CCKbR* probe (accession number
450 NM_007627.4, probe region 136-1164). After hybridization, the brain sections went
451 through 4 steps of signal amplification fluorescent label. Anti-DsRed or GFP staining
452 was performed after the RNAscope staining. Slides were imaged with a confocal
453 microscope (Olympus FluoView FV1200).
454

455 **Stereotaxic injections and optical fiber/cannula implantation**

456 For surgical procedures, mice were anaesthetized with sodium pentobarbital (0.1 g/kg)
457 and placed in a stereotaxic apparatus (RWD). Stereotaxic surgery was performed as
458 described (Li Sun et al., 2020). Briefly, holes were made into the skull over the target
459 areas to inject the virus with glass pipettes (diameter,10-15 mm) or to implant optical
460 fibers [outer diameter (o.d.): 200 μm; length: 6.0 mm, 0.37 NA; Inper] or to implant of
461 guide cannula [outer diameter (o.d.): 0.41 mm; RWD]. The coordinates relative to
462 bregma were as follows according to the Paxinos and Franklin (2001) atlas. For all

463 experiments, mice with incorrect injection sites were excluded from further analysis.

464 For optical activation of LPB^{CCK} neurons, AAV2/9-hEF1a-DIO-hChR2(H134R)-

465 EYFP-WPRE-pA(viral titers: 2.95×10^{13} particles/ml; Taitool Bioscience) or AAV2/9-

466 hEF1a-DIO-EYFP-WPRE-pA (viral titers: 1.0×10^{12} particles/ml; Taitool Bioscience)

467 virus was unilaterally microinjected into the LPB (AP: -4.8; ML: -1.35; DV: -3.4; mm

468 relative to bregma) of CCK-Cre mice. The virus was diluted into 5.9×10^{12} genomic

469 copies per ml with phosphate-buffered saline (PBS) before use and injected with 65 nl

470 into the LPB. Virus was delivered at a flow rate of 10 nl/min. The glass capillary was

471 left in place for an additional 10 min after injection to allow diffusion of the virus. The

472 cannulas were held in place with dental cement above the LPB (AP: -4.8; ML: -1.35;

473 DV: -3.2; mm relative to bregma).

474 For optical activation of PVN^{Vglut2} neurons, AAV2/9-EF1a-DIO-hChR2-EYFP

475 (viral titers: 2.95×10^{13} particles/ml; Taitool Bioscience) or AAV2/9-EF1α-DIO-

476 EYFP (viral titers: 1.0×10^{12} particles/ml; Taitool Bioscience) virus was unilaterally

477 microinjected into the PVN (AP: -0.4; ML: -0.15; DV: -4.95; mm relative to bregma)

478 of Vglut2-Cre mice. The virus was diluted into 2.0×10^{12} genomic copies per ml with

479 PBS before use and injected with 70 nl into the PVN. Virus was delivered at a flow rate

480 of 15 nl/min. The glass capillary was left in place for an additional 10 min after injection

481 to allow diffusion of the virus. The cannulas were held in place with dental cement

482 above the PVN (AP: -0.4; ML: -0.15; DV: -4.75; mm relative to bregma).

483 For optical activation of PVN^{CRH} neurons, AAV2/9-EF1a-DIO-hChR2-EYFP

484 (viral titers: 2.95×10^{13} particles/ml; Taitool Bioscience) or AAV2/9-EF1α-DIO-

485 EYFP (viral titers: 1.0×10^{12} particles/ml ; Taitool Bioscience) was unilaterally
486 microinjected into the PVN (AP: -0.4; ML: -0.15; DV: -4.90 mm relative to bregma) of
487 CRH-Cre mice. The virus was diluted into 4.0×10^{12} genomic copies per ml with PBS
488 before use and injected with 75 nl into the PVN. Virus was delivered at a flow rate of
489 15 nl/min. The glass capillary was left in place for an additional 10 min after injection
490 to allow diffusion of the virus. The cannulas were held in place with dental cement
491 above the PVN (AP: -0.4; ML: -0.15; DV: -4.7; mm relative to bregma).

492 For optical inhibition of LPB^{CCK} neurons, AAV2/9-EF1α-DIO-hGtACR1-P2A-
493 eYFP-WPRE (5×10^{13} particles/ml; Taitool Bioscience) or AAV2/9-hEF1a-DIO-
494 EYFP-WPRE-pA (viral titers: 1.0×10^{12} particles/ml; Taitool Bioscience) virus was
495 bilaterally infused to the LPB (AP: -4.8; ML: -1.35; DV: -3.4; mm relative to bregma)
496 of CCK-Cre mice. The virus was diluted into 1.67×10^{12} genomic copies per ml with
497 PBS before use and injected with 70 nl into the LPB. Optical fibers were bilaterally
498 implanted at an angle of 5° above the LPB (AP: -4.8; ML: -1.72; DV: -2.94; mm relative
499 to bregma).

500 In order to study the downstream of LPB^{CCK} neurons, AAV2/9-hSyn-DIO-mGFP-
501 2A-Synaptophysin-mRuby (viral titers: 1.55×10^{13} particles/ml; Taitool Bioscience)
502 virus was unilaterally injected into the LPB (AP: -4.8 mm; ML: -1.35 mm; DV: -3.4
503 mm) of CCK-Cre mice; in order to study the source of CCKergic upstream of PVN,
504 AAV2/2-Retro-hEF1a-DIO-EYFP-WPRE-pA (viral titers: 2.52×10^{13} particles/ml;
505 Taitool Bioscience) virus was unilaterally injected into the PVN (AP, -0.4 mm; ML, -
506 0.2mm; DV, -4.85mm) of CCK-Cre mice.

For LPB^{CCK}-PVN axon terminal stimulation, AAV2/9-hEF1a-DIO-hChR2(H134R)-EYFP-WPRE-pA (viral titers: 2.95 × 10^{13} particles/ml; Taitool Bioscience) or AAV2/9-hEF1a-DIO-EYFP-WPRE-pA (viral titers: 1.0×10^{12} particles/ml; Taitool Bioscience) virus was unilaterally microinjected into the LPB (AP: -4.8; ML: -1.35; DV: -3.4; mm relative to bregma) of CCK-Cre mice. The virus was diluted into 5.9×10^{12} genomic copies per ml with PBS before use and injected with 65 nl into the LPB. After the virus was expressed for 2 weeks, for LPB^{CCK}-PVN axon terminals stimulation, optical fibers were unilaterally implanted above the PVN (AP: -0.4; ML: -0.2; DV: -4.7; mm relative to bregma).

For pharmacological experiments (procedures of optical activation of LPB^{CCK} neurons have been mentioned above), drug cannulas were ipsilaterally implanted into the PVN (AP, -0.4 mm; ML, -0.2mm; DV, -4.7mm).

For prolonged inhibition of PVN neurons, AAV2/9-hSyn-mCherry-WPRE-pA (viral titers: ≥1.0 × 10^{13} particles/ml; Taitool Bioscience) or AAV2/9-hSyn-hM4D(Gi)-mCherry-WPRE-pA(viral titers: ≥1.0×10^{13} particles/ml; Taitool Bioscience) virus was microinjected into the PVN (AP, -0.4 mm; ML, -0.2mm; DV, -4.85mm) of CCK-Cre mice.

For fiber photometry experiments, AAV2/9-hSyn-DIO-GCaMP7s-WPRE virus (viral titers: 2.0 × 10^{12} particles/ml; Taitool Bioscience) were injected into the LPB of CCK-ires-Cre mice. After two weeks, an optical fiber was implanted into the LPB, then each mouse was allowed to recover for 1 week before recording. Each mouse was handled for 3 days prior to fiber photometry recording.

529

530 **Fiber photometry**

531 Mice were allowed to recover from surgery for at least 7 days before the behavioral
532 experiments. The fiber photometry system (RWD Life Science Co., Ltd, China) was
533 used for recording fluorescence signal (GCaMP7s and isosbestic wavelengths) which
534 produced by an exciting laser beam from 470 nm LED light and 410nm LED light.
535 Calcium fluorescence signals were acquired at 60Hz with alternating pluses of 470 nm
536 and 410 nm light. The power at the end of the optical fiber (200μm, 0.37NA, 2m) was
537 adjusted to 20 μW. Recording parameters were set based on pilot studies that
538 demonstrated the least amount of photobleaching, while allowing for the sufficient
539 detection of the calcium response. We used the camera for behavioral video recordings
540 to synchronize calcium recordings. On the experimental day, mice were allowed to
541 acclimate in the home cage for 30 min. Regarding quantification, the filtered 410 nm
542 signal was aligned with the 470 nm signal by using the least-square linear fit. ΔF/F was
543 calculated according to (470 nm signal-fitted 410 nm signal)/(fitted 410 nm signal).
544 And the standard z-score calculation method is used, that is, Z-score = (x-mean)/std, x
545 = △F/F. During the behavior experiments, the GCaMP7s fluorescence intensity was
546 recorded.

547

548 **In vivo optogenetic manipulation**

549 For optogenetic manipulation experiments, an implanted fiber was connected to a 473
550 nm laser power source (Newdoon Inc., Hangzhou, China). The power of the blue (473
551 nm) (Newdoon Inc., Hangzhou, China) was 0.83-3.33 mW mm^2 as measured at the tip

552 of the fiber. 473 nm laser (ChR2: power 5-15 mW, frequency 20 Hz, pulse width 5 ms;
553 GtACR1: power 15 mW, direct current) was supplied to activate or inhibit neurons,
554 respectively.
555
556 **Pharmacological antagonism**
557 Antagonists were delivered 30 min before optical activation of LPB^{CCK} neurons. For
558 blocking glutamatergic neurotransmission, we firstly connected guiding cannula with a
559 Hamilton syringe via a polyethylene tube. Then we infused 0.25 μl mixed working
560 solution containing CNQX disodium salt hydrate (0.015 μg; Sigma-Aldrich), a
561 glutamate AMPA receptor antagonist, and AP5 (0.03 μg; Sigma-Aldrich), a NMDA
562 receptor antagonist, into the PVN with a manual microinfusion pump (RWD, 68606)
563 over 5 min. For blocking CCKergic neurotransmission, 0.25 μl mixed solution
564 containing Devazepide (0.0625 μg; Sigma-Aldrich), a CCKaR receptor antagonist, and
565 L-365,260(0.0625 μg; Sigma-Aldrich), a CCKbR receptor antagonist, was infused into
566 the PVN over a period of 5 min. To prevent backflow of fluid, the fluid-delivery cannula
567 was left for 10 min after infusion.
568
569 **Chemogenetic manipulation**
570 Clozapine Noxide (CNO, Sigma) was dissolved in saline (5 mg in 10 uL DMSO & 190
571 uL 0.9% NaCl solution). CNO was injected intraperitoneally at 0.3 mg per kg of body
572 weight for chemogenetic manipulation.
573

574 **C-fos staining and analysis**

575 For c-fos quantification, mice were perfused 1.5 h after 10 min blue photostimulation
576 illumination, and sections were cut. The boundaries of the nuclei were defined
577 according to brain atlases Mouse Brain Atlas (Franklin and Paxinos, 2008). Cell
578 counting was carried out manually.

579

580 **Behavioral task**

581 For all behavioral tests, experimenters were blinded to genotypes and treatments. Mice
582 were handled daily at least seven days before performing behavioral tests. All the
583 apparatuses and cages were sequentially wiped with 70% ethanol and ddH_2O then air-
584 dried between stages. At the end of behavioral tests, mice were perfused with 4% PFA
585 followed by post hoc analysis to confirm the viral injection sites, optic fiber and cannula
586 locations. Mice with incorrect viral injection sites, incorrect positioning of optical fibers
587 or cannula were excluded.

588

589 **Real-time place aversion test**

590 Mice were habituated to a custom-made 20 × 30 × 40 cm two-chamber apparatus
591 (distinct wall colors and stripe patterns) before the test. First stage: each mouse was
592 placed in the center and allowed to explore both chambers without laser stimulation for
593 10 min. After exploration, the mouse indicated a small preference for one of the two
594 chambers. Second stage: 473 nm laser stimulation (20 Hz, 8 mW, 5 ms) was delivered

595 when the mouse entered or stayed in the preferred chamber, and the light was turned
596 off when the mouse moved to the other chamber for 10 min.
597
598 **Flight-to-nest test**
599 Flight-to-nest test was performed using previously described methods (Zhou, Z., et al,
600 2019). Flight-to-nest test was performed in a 40 × 40 × 30 cm closed box with a 27-
601 inch LED monitor stationed on top to display the stimulus. A nest in the shape of a 20
602 cm wide × 12 cm high triangular prism was in the corner of the closed Plexiglas box.
603 There are two cameras, one from the top, one from the side (Logitech) that record the
604 mouse's activity simultaneously. Briefly, on day 1, the mice were habituated to the box
605 conditions for 15 min. On day 2, the mice were first allowed to explore the box for 5-
606 10 min. When the mice were in the corner furthest from the nest and within in a body-
607 length distance from the wall, they were given optical stimulus. For optogenetic
608 activation of LPB^{CCK} neurons or LPB^{CCK}-PVN experiments, mice received a 20 s 473
609 nm blue laser (frequency 20 Hz, pulse width 5 ms) with 15-20 mW (terminal) or 5-10
610 mW (soma) light power at the fiber tips. For prolonged inhibition of PVN neurons,
611 Clozapine Noxide (CNO, Sigma-Aldrich) was dissolved in saline to a concentration of
612 3 mg/ml. The flight-to-nest test was performed 1.5 h after CNO intraperitoneally
613 injection.
614
615 **Flight-to-nest behavioral analysis**

The behaviors of the mice were recorded and analyzed automatically with Anymaze software (Global Biotech Inc). Behavioral analysis was performed as previously described (Zhou, Z., et al, 2019). Flight-to-nest behavior was characterized on the basis of the three aspects: latency to return nest, speed (% of baseline speed), time spent in nest (% of 2 min). Latency to return nest refers to the moment from optical stimulus onset to moment when the mouse first went into the nest. Speed (% of baseline speed) refers to the ratio of the post-stimulation speed to the baseline speed. We recorded the speed of the mice in the 50 seconds before photostimulation presentation as the baseline speed. The post-stimulation speed was record from the time of stimulation to 15 s after. It was averaged over a 1 s time window centered on the maximum speed. Time spent in nest (% of 2 min) refers to the time from mouse's body was first completely under the shelter after photostimulation to the time when the mouse left the nest.

Open field test

The open-field chamber was made of plastic (50 × 50 × 50 cm). At the start of the test, mice were placed in the periphery of the open-field chamber. The open field test lasted 5min.

Elevated plus-maze test

The elevated plus maze was made of plastic with two open arms (30 × 5 cm), two closed arms (30 × 5 × 30 cm) and a central platform (5 × 5 × 5 cm). At the beginning of the experiments, mice were placed in the center platform facing a closed arm. The elevated plus-maze test lasted 5 min.

Heart rate measurements

Heart rate was measured via a pulse oximeter (MouseOx Plus; Starr Life Sciences). Mice were placed in the home cage with a detector fixed around the neck. After habituation for 10 min, heart rate was simultaneously measured for 10 min while intermittent 2 min period blue light was applied. Each mouse was tested 3 times, and the mean heart rate was calculated. Heart rate data was analyzed with the MouseOx Plus Conscious Applications Software.

Pupil size measurements

Mice were adapted to constant room light (100 lx) for 1 h before testing. Mice were kept unanaesthetized and restrained in a stereotaxic apparatus during the experiment. The pupil size was recorded using Macro module camera under constant light conditions before stimulation, during stimulation, and after stimulation. The test lasted 90 s, consisting of 30 s light off-on-off epochs. The pupil size was later measured by Matlab software.

Heat exposure assay

We used a translucent plastic box (38 × 25 cm) divided into two parts, the smaller part is the unheated comfortable zone (5 × 25 cm), and the larger part with rubber heating pad is the hot uncomfortable zone (33 × 25 cm). The rubber heating pad was heated to 43℃, and the heat insulated pad was placed in the comfortable zone to avoid the heat.

The heating temperature 43℃ was chosen because it would cause heat escape but not heat pain (W. Wang, P. J. Schuette, J. Nagai, et al., 2021; Weisheng et al., 2021).

Rat exposure assay

We used a rectangular chamber (70 × 25 × 30 cm). Mice were acclimated to this environment for three days for 10 minutes each day. During the rat exposure period, a live rat was restrained to one end of the chamber using a harness attached to the chamber wall. As a control, before a live rat exposure, we exposed mice to a toy rat (similar in size and shape to a live rat). For fiber photometry recordings, all mice underwent rat exposure for 20 minutes. For photoinhibition tests, mice were exposed to live rat and all trials lasted 10 min.

Looming test

The looming test was performed in a closed Plexiglas box (40 × 40 × 30 cm) with a shelter in the corner. For looming stimulation, an LCD monitor was placed on the ceiling to present multiple looming stimuli, which was a black disc expanding from a visual angle of 2° to 20° in 0.5 s. The expanding disc stimulus was repeated for 20 times in quick succession and each repeat is followed by a 0.15 s pause. Animals were habituated for 10-15 min in the looming box one day before testing. During the looming test, mice were first allowed to freely explore for 3-5 min. For calcium signal experiment, total 5 trials of looming stimuli were presented and analyzed. Behavior was recorded for 20 minutes. For photoinhibition tests, light stimulation was given 1 s before the looming stimulus appears and continue until the looming stimulus ends.

684

685 **TMT odor test**

686 During this test, all mice were habituated to the testing environment for three days
687 before any experimental manipulation. For the photometry studies involving odor
688 presentations, mice were placed on a plastic chamber (30 × 30 × 20 cm). A dish
689 (diameter, 5 cm) with cotton was positioned on the side beside the chamber. When TMT
690 (Ferro Tec, 4 ul of 100%) was used as the stimulus, cotton was first wetted with the
691 equivalent volume of 0.1 M PBS. After a habituation period, the dish was replaced with
692 a new one scented with the TMT. The mice were free to explore in the chamber, and
693 behavior was recorded for 20 minutes.

694

695 **Measurements of corticosterone**

696 Blood samples were collected to determine the hormone levels. Taking Blood was
697 performed in the morning by rapidly collecting heart blood after anesthetization. We
698 immediately collected blood after 10 min of light stimulation (10 mw, 20 Hz, 5 ms pulse
699 width, 15 s per min, 473 nm). Blood samples were temporarily placed in iced plastic
700 tubes coated with heparin. All serum was prepared after every blood sample was
701 centrifuged at 2000 g for 2.5 min at 4°C. Supernatant was collected and plasma
702 corticosterone concentration was measured using commercially-available ELISA kits
703 (Enzo ADI-900-097).

704

705 **In vitro electrophysiology**

706 Each mouse was anesthetized with pentobarbital sodium (100 mg/kg, i.p.) and

707 decapitated. Then the whole brain was quickly dissected into ice-cold oxygenated (95%
708 O_2 and 5% CO_2) artificial cerebrospinal fluid (aCSF) (93 mM N-methyl-D-glucamine,
709 2.5 mM KCl, 1.2 mM NaH_2PO_4, 20 mM HEPES, 25 mM D-glucose, 30 mM $NaHCO_3$,
710 10 mM $MgSO_4$, 0.5 mM $CaCl_2$, 5 mM sodium ascorbate, 3 mM sodium pyruvate, and
711 1 mM kynurenic acid), followed by cutting coronally into 300 μm slices on a microtome
712 (VTA-1200S; Leica). Slices containing the LPB were transferred to a similar solution
713 (93 mM NaCl, 2.5 mM KCl, 1.2 mM NaH_2PO_4, 20 mM HEPES, 25 mM D-glucose, 30
714 mM $NaHCO_3$, 2 mM $MgSO_4$, 2 mM $CaCl_2$, 5 mM sodium ascorbate, 3 mM sodium
715 pyruvate, and 1 mM kynurenic acid), and incubated for at lowest 1 h at room
716 temperature (24-26°C). Then the brain slices were transferred to a recording chamber
717 attached to the fixed stage of an BX51WI microscope (Olympus) (solution containing:
718 125 mM NaCl, 3 mM KCl, 1.25 mM NaH_2PO_4, HEPES, 10 mM D-glucose, 26 mM
719 $NaHCO_3$, 2 mM $MgSO_4$ and 2 mM $CaCl_2$). Patch glass electrodes were pulled from
720 borosilicate capillaries (BF150-86-10; Sutter Instrument Co, Novato, CA, USA) and
721 filled with artificial intracellular fluid following component: 135 mM $CsMeSO_3$, 10
722 mM HEPS, 0.5 mM EGTA, 3.3 mM QX-314, 4 mM Mg-ATP, 0.3 mM Na_2-GTP, 8 mM
723 Na_2-Phosphocreatine. Whole-cell voltage-clamp recordings were made with a
724 MultiClamp 700B amplifier (Molecular Devices). To tested the efficacy of ChR2-
725 mediated activation, LED-generated blue light pulses were applied to recorded neurons
726 using 4 different frequencies (5,10, 20, and 40 Hz). To test the effects of photoactivation
727 of LPB^{CCK} projection terminals within PVN, blue light pulses were applied to the
728 recorded PVN neurons. To confirm that postsynaptic currents were monosynaptic, the

729 blue light-evoked currents were recorded in the presence of ACSF (Ctrl), TTX (1 μM)
730 and 4-AP (100 μM). To confirm that postsynaptic currents were monosynaptic. CNQX
731 (20 μM) and AP5 (50 μM) were perfused with ACSF to examine the neurotransmitter
732 type used on LPB^{CCK}-PVN projection. Signals were low-pass filtered at 10 kHz and
733 digitized at 10 kHz (MICRO3 1401, Cambridge Electronic Design). Data were acquired
734 and analyzed using Spike2 7.04 software (Cambridge Electronic Design).
735

736 **Quantification and statistical analysis**

737 All data analyses were conducted blinded. All statistical analyses were performed with
738 GraphPad Prism (version 7.0) and analyzed by Unpaired Student's t-tests, one-way
739 ANOVA, two-way ANOVA according to the form of the data. Nonparametric tests were
740 used if the data did not match assumed Gaussian distribution. Animals were randomly
741 assigned to treatment groups. All data were presented as Mean ± SEM, with statistical
742 significance taken as $*p < 0.05$, $**p < 0.01$ and $***p < 0.001$.
743

744 **Acknowledgements**

745 We thank Weisheng Wang, Xiaoming Li, Bin Zhang, Zhi Chen, Yu-dong Zhou, Kai Liu,
746 Huifang Lou for technical support. This work was supported by the National Key
747 Research and Development Program (2021ZD0202700 and 2021ZD0202703), the
748 Leading talents in Science and Technology of Zhejiang Province (2021R52021), the
749 National Natural Science Foundation of China (82090033), the NSFC-Guangdong Joint
750 Fund (U20A6005), the Key Research and Development Program of Zhejiang province

(2020C03009 and 2020R01001), the Research Units for Emotion and Emotion Disorders, Chinese Acedemy of Medical Sciences (2019-I2M-5-057), the Key Realm R&D Program of Guangdong province (2019B030335001).

Author contributions

Fan Wang, Yuge Chen, conceptualization, experimental design and execution, data collection and curation, manuscript writing and revision; Yuxin Lin, Xuze Wang, experimental execution, data collection; Kaiyuan Li, Jintao Wu electrophysiology recording; Yong Han, Zhenggang Zhu, Xiaojun Hu, technical support; Xingyi Shi, Chaoying Long, data analyses; Zhihua Gao, Shumin Duan, conceptualization, project administration, experimental design, data curation, funding acquisition, manuscript writing, revision and editing.

Declaration of interests

The authors declare no competing interests.

References

Anderson, D. J., & Adolphs, R. (2014). A framework for studying emotions across species. Cell, 157(1), 187-200. doi:10.1016/j.cell.2014.03.003

Bertoglio, L. J., de Bortoli, V. C., & Zangrossi, H., Jr. (2007). Cholecystokinin-2 receptors modulate freezing and escape behaviors evoked by the electrical stimulation of the rat dorsolateral periaqueductal gray. Brain Res, 1156, 133-138. doi:10.1016/j.brainres.2007.04.038

Blanchard, D. C., Griebel, G., & Blanchard, R. J. (2001). Mouse defensive behaviors: pharmacological and behavioral assays for anxiety and panic. Neurosci Biobehav Rev, 25(3), 205-218. doi:10.1016/s0149-7634(01)00009-4

Blanchard, D. C., Griebel, G., & Blanchard, R. J. (2001). Mouse defensive behaviors: pharmacological and behavioral assays for anxiety and panic. Neuroscience & Biobehavioral Reviews, 25(3), 205-218.

Campos, C. A., Bowen, A. J., Roman, C. W., & Palmiter, R. D. (2018). Encoding of danger by parabrachial CGRP neurons. Nature, 555(7698), 617-622.

Canteras, N. S., Ribeiro-Barbosa, E. R., & Comoli, E. (2001). Tracing from the dorsal premammillary nucleus prosencephalic systems involved in the organization of innate fear responses. Neurosci Biobehav Rev, 25(7-8), 661-668. doi:10.1016/s0149-7634(01)00048-3

Chen, L., Liu, Y., Su, P., Hung, W., Li, H., Wang, Y., . . . Gao, S. (2022). Escape steering by cholecystokinin peptidergic signaling. Cell Rep, 38(6), 110330. doi:10.1016/j.celrep.2022.110330

Chiang, M. C., Bowen, A., Schier, L. A., Tupone, D., Uddin, O., & Heinricher, M. M. (2019). Parabrachial Complex: A Hub for Pain and Aversion. J Neurosci, 39(42), 8225-8230. doi:10.1523/JNEUROSCI.1162-19.2019

Cooper Jr, W. E., & Blumstein, D. T. (2015). Escaping From Predators: Escape decisions prior to pursuit.

Coote, J. H. (2005). A role for the paraventricular nucleus of the hypothalamus in the autonomic control of heart and kidney. Exp Physiol, 90(2), 169-173.

doi:10.1113/expphysiol.2004.029041

Crawford, M., & Masterson, F. A. (1982). Species-specific defense reactions and avoidance learning. An evaluative review. Pavlov J Biol Sci, 17(4), 204-214. doi:10.1007/bf03001275

Daviu, N., Füzesi, T., Rosenegger, D. G., Rasiah, N. P., Sterley, T.-L., Peringod, G., & Bains, J. S. (2020). Paraventricular nucleus CRH neurons encode stress controllability and regulate defensive behavior selection. Nature neuroscience, 23(3).

Daviu, N., Fuzesi, T., Rosenegger, D. G., Rasiah, N. P., Sterley, T. L., Peringod, G., & Bains, J. S. (2020). Paraventricular nucleus CRH neurons encode stress controllability and regulate defensive behavior selection. Nat Neurosci, 23(3), 398-410. doi:10.1038/s41593-020-0591-0

Day, H. E., Masini, C. V., & Campeau, S. (2004). The pattern of brain c-fos mRNA induced by a component of fox odor, 2,5-dihydro-2,4,5-trimethylthiazoline (TMT), in rats, suggests both systemic and processive stress characteristics. Brain Res, 1025(1-2), 139-151. doi:10.1016/j.brainres.2004.07.079

Day, H. E., Masini, C. V., & Campeau, S. (2004). The pattern of brain c-fos mRNA induced by a component of fox odor, 2, 5-dihydro-2, 4, 5-trimethylthiazoline (TMT), in rats, suggests both systemic and processive stress characteristics. Brain research, 1025(1-2), 139-151.

Dong, P., Wang, H., Shen, X. F., Jiang, P., Zhu, X. T., Li, Y., . . . Li, X. M. (2019). A novel cortico-intrathalamic circuit for flight behavior. Nat Neurosci, 22(6), 941-

949. doi:10.1038/s41593-019-0391-6

Eilam, D. (2005). Die hard: a blend of freezing and fleeing as a dynamic defense--implications for the control of defensive behavior. Neurosci Biobehav Rev, 29(8), 1181-1191. doi:10.1016/j.neubiorev.2005.03.027

Ellard, C. G., & Eller, M. C. (2009). Spatial cognition in the gerbil: computing optimal escape routes from visual threats. Animal Cognition, 12(2).

Fanselow, M. S., & Bolles, R. C. (1979). Naloxone and shock-elicited freezing in the rat. J Comp Physiol Psychol, 93(4), 736-744. doi:10.1037/h0077609

Faturi, C. B., Rangel, M. J., Jr., Baldo, M. V., & Canteras, N. S. (2014). Functional mapping of the circuits involved in the expression of contextual fear responses in socially defeated animals. Brain Struct Funct, 219(3), 931-946. doi:10.1007/s00429-013-0544-4

Ferguson, A. V., Latchford, K. J., & Samson, W. K. (2008). The paraventricular nucleus of the hypothalamus - a potential target for integrative treatment of autonomic dysfunction. Expert Opin Ther Targets, 12(6), 717-727. doi:10.1517/14728222.12.6.717

Fulwiler, C. E., & Saper, C. B. (1984). Subnuclear organization of the efferent connections of the parabrachial nucleus in the rat. Brain Research Reviews, 7(3), 229-259.

Fulwiler, C. E., & Saper, C. B. (1984). Subnuclear organization of the efferent connections of the parabrachial nucleus in the rat. Brain Res, 319(3), 229-259. doi:10.1016/0165-0173(84)90012-2

Garfield, A. S., Shah, B. P., Madara, J. C., Burke, L. K., Patterson, C. M., Flak, J., . . . Heisler, L. K. (2014). A parabrachial-hypothalamic cholecystokinin neurocircuit controls counterregulatory responses to hypoglycemia. Cell Metab, 20(6), 1030-1037. doi:10.1016/j.cmet.2014.11.006

Gross, C. T., & Canteras, N. S. (2012). The many paths to fear. Nat Rev Neurosci, 13(9), 651-658. doi:10.1038/nrn3301

Han, S., Mao, H., & Dally, W. J. (2015). Deep compression: Compressing deep neural networks with pruning, trained quantization and huffman coding. arXiv preprint arXiv:1510.00149.

Han, S., Soleiman, M. T., Soden, M. E., Zweifel, L. S., & Palmiter, R. D. (2015). Elucidating an Affective Pain Circuit that Creates a Threat Memory. Cell, 162(2), 363-374. doi:10.1016/j.cell.2015.05.057

Han, S., Soleiman, M. T., Soden, M. E., Zweifel, L. S., & Palmiter, R. D. (2015). Elucidating an Affective Pain Circuit that Creates a Threat Memory. Cell, 162(2).

Isosaka, T., Matsuo, T., Yamaguchi, T., Funabiki, K., Nakanishi, S., Kobayakawa, R., & Kobayakawa, K. (2015). Htr2a-expressing cells in the central amygdala control the hierarchy between innate and learned fear. Cell, 163(5), 1153-1164.

Keay, K. A., & Bandler, R. (2001). Parallel circuits mediating distinct emotional coping reactions to different types of stress. Neurosci Biobehav Rev, 25(7-8), 669-678. doi:10.1016/s0149-7634(01)00049-5

Kim, J., Lee, S., Fang, Y.-Y., Shin, A., Park, S., Hashikawa, K., . . . Lin, D. (2019).

Rapid, biphasic CRF neuronal responses encode positive and negative valence. Nature neuroscience, 22(4), 576-585.

Krout, K. E., & Loewy, A. D. (2000). Parabrachial nucleus projections to midline and intralaminar thalamic nuclei of the rat. John Wiley & Sons, Ltd, 428(3).

La-Vu, M., Sethi, E., Maesta-Pereira, S., Schuette, P. J., Tobias, B. C., Reis, F. M., . . . Adhikari, A. (2022). A genetically-defined population in the lateral and ventrolateral periaqueductal gray selectively promotes flight to safety. bioRxiv.

LeDoux, J. (2012). Rethinking the Emotional Brain (vol 73, pg 653, 2012). Neuron, 73(5), 1052-1052. doi:10.1016/j.neuron.2012.02.018

Li, S., Rui, L., Fang, G., ManQing, W., XiaoLin, M., KaiYuan, L., . . . Shumin, D. (2020). Parabrachial nucleus circuit governs neuropathic pain-like behavior. Nature communications, 11(1).

Lin, S., Zhu, M.-Y., Tang, M.-Y., Wang, M., Yu, X.-D., Zhu, Y., . . . Li, X.-M. (2022). Somatostatin-Positive Neurons in the Rostral Zona Incerta Modulate Innate Fear-Induced Defensive Response in Mice. Neuroscience Bulletin, 1-16.

Liu, S., Ye, M., Pao, G. M., Song, S. M., Jhang, J., Jiang, H., . . . Han, S. (2022). Divergent brainstem opioidergic pathways that coordinate breathing with pain and emotions. Neuron, 110(5), 857-873. e859.

Liu, X., Dimidschstein, J., Fishell, G., & Carter, A. G. (2020). Hippocampal inputs engage CCK+ interneurons to mediate endocannabinoid-modulated feed-forward inhibition in the prefrontal cortex. Elife, 9. doi:10.7554/eLife.55267

Mangieri, L. R., Jiang, Z., Lu, Y., Xu, Y., Cassidy, R. M., Justice, N., . . . Tong, Q.

(2019a). Defensive Behaviors Driven by a Hypothalamic-Ventral Midbrain Circuit. eNeuro, 6(4). doi:10.1523/ENEURO.0156-19.2019

Mangieri, L. R., Jiang, Z., Lu, Y., Xu, Y., Cassidy, R. M., Justice, N., . . . Tong, Q. (2019b). Defensive Behaviors Driven by a Hypothalamic-Ventral Midbrain Circuit. eNeuro, 6(4), ENEURO.0156-0119.2019. doi:10.1523/ENEURO.0156-19.2019

Martinez, R. C., Carvalho-Netto, E. F., Amaral, V. C., Nunes-de-Souza, R. L., & Canteras, N. S. (2008). Investigation of the hypothalamic defensive system in the mouse. Behav Brain Res, 192(2), 185-190. doi:10.1016/j.bbr.2008.03.042

Meister, B., Broberger, C., Villar, M. J., & Hökfelt, T. (1994). Cholecystokinin B receptor gene expression in hypothalamic neurosecretory neurons after experimental manipulations. Neuroendocrinology, 60(5), 458-469.

Mileikovskii, B., & Verevkina, S. V. (1991). Influence of brain stem structures on the formation of the defensive behavior of animals. Neurosci Behav Physiol, 21(2), 126-130. doi:10.1007/bf01182887

O'Shea, R. D., & Gundlach, A. L. (1993). Regulation of cholecystokinin receptors in the hypothalamus of the rat: reciprocal changes in magnocellular nuclei induced by food deprivation and dehydration. J Neuroendocrinol, 5(6), 697-704. doi:10.1111/j.1365-2826.1993.tb00542.x

Olivier, B., Mos, J., & Slangen, J. L. (1991). Animal models in psychopharmacology: Springer.

Penzo, M. A., Robert, V., Tucciarone, J., De Bundel, D., Wang, M., Van Aelst, L., . . .

He, M. (2015). The paraventricular thalamus controls a central amygdala fear circuit. Nature, 519(7544), 455-459.

Perusini, J. N., & Fanselow, M. S. (2015). Neurobehavioral perspectives on the distinction between fear and anxiety. Learn Mem, 22(9), 417-425. doi:10.1101/lm.039180.115

Reis, F. M., Lee, J. Y., Maesta-Pereira, S., Schuette, P. J., Chakerian, M., Liu, J., . . . Kihara, A. H. (2021). Dorsal periaqueductal gray ensembles represent approach and avoidance states. Elife, 10, e64934.

Salay, L. D., Ishiko, N., & Huberman, A. D. (2018). A midline thalamic circuit determines reactions to visual threat. Nature, 557(7704), 183-189. doi:10.1038/s41586-018-0078-2

Saper, C., & Loewy, A. (1980). Efferent connections of the parabrachial nucleus in the rat. Brain research, 197(2), 291-317.

Shen, C. J., Zheng, D., Li, K. X., Yang, J. M., Pan, H. Q., Yu, X. D., . . . Li, X. M. (2019). Cannabinoid CB(1) receptors in the amygdalar cholecystokinin glutamatergic afferents to nucleus accumbens modulate depressive-like behavior. Nat Med, 25(2), 337-349. doi:10.1038/s41591-018-0299-9

Staples, L. G., McGregor, I. S., Apfelbach, R., & Hunt, G. E. (2008). Cat odor, but not trimethylthiazoline (fox odor), activates accessory olfactory and defense-related brain regions in rats. Neuroscience, 151(4), 937-947. doi:10.1016/j.neuroscience.2007.11.039

Sun, L., Liu, R., Guo, F., Wen, M. Q., & Duan, S. (2020). Parabrachial nucleus circuit

governs neuropathic pain-like behavior. Nature communications, 11(1).

Sun, L., Liu, R., Guo, F., Wen, M. Q., Ma, X. L., Li, K. Y., . . . Duan, S. (2020). Parabrachial nucleus circuit governs neuropathic pain-like behavior. Nat Commun, 11(1), 5974. doi:10.1038/s41467-020-19767-w

Sun, X. C., Bernstein, M. J., Meng, M. Z., Rao, S. Y., Sorensen, A. T., Yao, L., . . . Lin, Y. X. (2020). Functionally Distinct Neuronal Ensembles within the Memory Engram. Cell, 181(2), 410-+. doi:10.1016/j.cell.2020.02.055

Sutton, A. K., Myers, M. G., Jr., & Olson, D. P. (2016). The Role of PVH Circuits in Leptin Action and Energy Balance. Annu Rev Physiol, 78(1), 207-221. doi:10.1146/annurev-physiol-021115-105347

Tokita, K., Inoue, T., & Boughter Jr, J. D. (2009). Afferent connections of the parabrachial nucleus in C57BL/6J mice. Neuroscience, 161(2), 475-488.

Tovote, P., Meyer, M., Ronnenberg, A., Ogren, S. O., Spiess, J., & Stiedl, O. (2005). Heart rate dynamics and behavioral responses during acute emotional challenge in corticotropin-releasing factor receptor 1-deficient and corticotropin-releasing factor-overexpressing mice. Neuroscience, 134(4), 1113-1122. doi:10.1016/j.neuroscience.2005.05.027

Vianna, D. M., Landeira-Fernandez, J., & Brandão, M. L. (2001). Dorsolateral and ventral regions of the periaqueductal gray matter are involved in distinct types of fear. Neurosci Biobehav Rev, 25(7-8), 711-719. doi:10.1016/s0149-7634(01)00052-5

Vong, L., Ye, C., Yang, Z., Choi, B., Chua, S., Jr., & Lowell, B. B. (2011). Leptin action

on GABAergic neurons prevents obesity and reduces inhibitory tone to POMC neurons. Neuron, 71(1), 142-154. doi:10.1016/j.neuron.2011.05.028

Wang, L., Chen, I. Z., & Lin, D. (2015). Collateral pathways from the ventromedial hypothalamus mediate defensive behaviors. Neuron, 85(6), 1344-1358. doi:10.1016/j.neuron.2014.12.025

Wang, W., Schuette, P. J., La-Vu, M. Q., Torossian, A., Tobias, B. C., Ceko, M., . . . Adhikari, A. (2021). Dorsal premammillary projection to periaqueductal gray controls escape vigor from innate and conditioned threats. Elife, 10. doi:10.7554/eLife.69178

Wang, W., Schuette, P. J., Nagai, J., Tobias, B. C., Cuccovia, V. R. F. M., Ji, S., . . . Adhikari, A. (2021). Coordination of escape and spatial navigation circuits orchestrates versatile flight from threats. Neuron, 109(11), 1848-1860 e1848. doi:10.1016/j.neuron.2021.03.033

Wang, W., Schuette, P. J., Nagai, J., Tobias, B. C., Reis, F. M. C. V., Ji, S., . . . Chakerian, M. (2021). Coordination of escape and spatial navigation circuits orchestrates versatile flight from threats. Neuron, 109(11), 1848-1860. e1848.

Weisheng, W., J., S. P., Jun, N., Christine, T. B., Midea, C. V. R. F., Shiyu, J., . . . Avishek, A. (2021). Coordination of escape and spatial navigation circuits orchestrates versatile flight from threats. Neuron(prepublish).

Whissell, P. D., Cajanding, J. D., Fogel, N., & Kim, J. C. (2015). Comparative density of CCK- and PV-GABA cells within the cortex and hippocampus. Frontiers in Neuroanatomy, 9, 124. doi:ARTN 124

10.3389/fnana.2015.00124

Xu, Y., Lu, Y., Cassidy, R. M., Mangieri, L. R., Zhu, C., Huang, X., . . . Tong, Q. (2019). Identification of a neurocircuit underlying regulation of feeding by stress-related emotional responses. Nat Commun, 10(1), 3446. doi:10.1038/s41467-019-11399-z

Xu, Y., Wu, Z., Sun, H., Zhu, Y., Kim, E. R., Lowell, B. B., . . . Tong, Q. (2013). Glutamate mediates the function of melanocortin receptor 4 on Sim1 neurons in body weight regulation. Cell Metab, 18(6), 860-870. doi:10.1016/j.cmet.2013.11.003

Yang, H., Yang, J., Xi, W., Hao, S., Luo, B., He, X., . . . Wang, H. (2016). Laterodorsal tegmentum interneuron subtypes oppositely regulate olfactory cue-induced innate fear. Nat Neurosci, 19(2), 283-289. doi:10.1038/nn.4208

Yang, W. Z., Du, X., Zhang, W., Gao, C., & Shen, W. L. (2020). Parabrachial neuron types categorically encode thermoregulation variables during heat defense.

Yilmaz, M., & Meister, M. (2013). Rapid innate defensive responses of mice to looming visual stimuli. Curr Biol, 23(20), 2011-2015. doi:10.1016/j.cub.2013.08.015

Yilmaz, M., & Meister, M. (2013). Rapid innate defensive responses of mice to looming visual stimuli. Current Biology, 23(20), 2011-2015.

Zhang, B., Wang, W., Zhang, Z., Hu, Y., Meng, F., Wang, F., . . . Gao, Z. (2018). Alternative Splicing of Disabled-1 Controls Multipolar-to-Bipolar Transition of Migrating Neurons in the Neocortex. Cereb Cortex, 28(10), 3457-3467. doi:10.1093/cercor/bhx212

Zhang, L., Hernández, V. S., & Eiden, L. E. (2020). Hindbrain PBN to CeC and ovBNST HiFi circuits modulate medial and lateral preoptic hypothalamus for defensive locomotion: the discovery of perisomatic PACAP-glutamatergic Calyx-of-Held-like synapse in the rodent pallidum nuclei. The FASEB Journal, 34(S1), 1-1.

1000 **Figure Legends**

1001 **Figure 1. Viral tracing and electrophysiology analyses of glutamatergic**
1002 **connections between LPB^{CCK} neurons and PVN neurons (A)** Scheme of viral
1003 strategy for retrograde tracing from the PVN in CCK-Cre mice using AAV2-Retro virus.
1004 **(B)** Representative image showing the injection site as marked by CTB555. **(C)**
1005 Representative histological images of EYFP^{+} neurons in the LPB. **(D-H)** A heatmap **(D)**
1006 demonstrating the distribution of EYFP^{+} neurons in the MO **(E)**, CC **(F)**, DI **(G)**, PAG
1007 **(H)**, n = 3 mice. **(I-J)** Anterograde tracing of LPB^{CCK} neurons using AAV-hSyn-FLEX-
1008 mGFP-2A-Synaptophysin-mRuby virus. **(K)** Projections of LPB^{CCK} neurons to the
1009 PVN. The right panel shows a magnified view of boxed area; scale bar, 100 μm; n = 3
1010 mice. **(L)** Schematic of recording from PVN cells after optogenetic activation of
1011 LPB^{CCK} axonal terminals. **(M)** Representative traces of light-evoked EPSCs recorded
1012 from PVN neurons following light stimulation of LPB^{CCK} axonal terminals in the
1013 presence of ACSF (Ctrl), TTX (1 μM) and 4-AP (100 μM). **(N)** Quantification of
1014 excitatory postsynaptic currents (EPSCs) from identified PVN neurons receiving inputs
1015 from the LPB^{CCK} neurons in the presence of ACSF (Ctrl), TTX (1 μM) and 4-AP (100
1016 μM). **(O)** Representative traces of light-evoked EPSCs recorded from PVN neurons
1017 following light stimulation of LPB^{CCK} axonal terminals in the presence of CNQX (20
1018 μM) and AP5 (50 μM) (n = 9 neurons). **(P)** Quantification of EPSCs and inhibitory
1019 postsynaptic currents (IPSCs) from identified PVN neurons receiving inputs from the
1020 LPB^{CCK} neurons.

1021

1022 **Figure 2. Activation of LPB^{CCK} neurons triggers defensive-like flight-to-nest**
1023 **behavior and autonomic responses. (A)** Left, schematic of light stimulation of and
1024 patch-clamp recording from ChR2-EYFP expressing CCK neurons in the LPB. Right,
1025 example of action potentials evoked by optogenetic stimulation LPB^{CCK} neurons using
1026 whole cell patch-clamp slice recording. **(B)** Schematic diagram of optogenetic
1027 activation of LPB^{CCK} neurons. **(C)** Representative image showing the ChR2-EYFP
1028 expression and optical fiber tip locations in the LPB of a CCK-Cre mouse. Scale bar,
1029 100 μm. **(D)** Schematic of the timing and behavioral paradigm with optical activation
1030 of LPB^{CCK} neurons. **(E-F)** Diagram of the real-time place aversion (RTPA) test and the
1031 example traces of the RTPA test from the mice. **(G) Q**uantification of the time of mice
1032 spent in the laser-paired chamber (EYFP: n = 5 mice, ChR2: n = 5 mice; df = 16; two-
1033 way ANOVA test) after optogenetic activation. **(H)** Diagram of the flight to nest test **(I-**
1034 **K)** Quantification of latency **(I),** speed **(J)** and time in the nest **(K)** (EYFP: n = 7 mice,
1035 ChR2: n = 7 mice; for latency, p = 0.0006, U = 0; Mann-Whitney test; for speed, p =
1036 0.0016, t = 4.052, df = 12; unpaired *t* test; for time in the nest, p < 0.0001, t = 19.82, df
1037 = 12; unpaired *t* test). **(L)** Analyses of heart rate changes induced by photostimulation
1038 of LPB^{CCK} neurons. (EYFP: n = 7 mice, ChR2: n = 7 mice; p = 0.0006, t = 4.603, df =
1039 12; unpaired *t* test). **(M-N)** Example images of computer-detected pupils **(M)** and
1040 quantitative analyses of pupil size before and during photo-stimulation of LPB^{CCK}
1041 neurons **(N)** (EYFP: n = 6 mice, ChR2: n = 6 mice; p = 0.0022, U = 0; Mann-Whitney
1042 test). **(O)** Cartoon of the arousal state during the activation of LPB^{CCK} neurons. **(P)**

1043 Plasma corticosterone levels in EYFP and ChR2 groups. (EYFP: n = 5 mice, ChR2: n
1044 = 5 mice; p = 0.0121, t = 3.23, df = 8; unpaired *t* test).
1045
1046 **Figure 3. Threat stimuli recruit LPB^{CCK} neurons to elicit defensive behaviors. (A)**
1047 Schematic of the *in vivo* recording system for the Ca^{2+} signal. **(B)** Schematic showing
1048 the injections and recording of LPB neurons in CCK-Cre mice. **(C)** A representative
1049 image (left panel) and a magnified view of neurons labeled by AAV-hsyn-DIO-
1050 GCaMP7s, scale bar, 100 μm; n = 5 mice. **(D)** Schematic of the rat exposure assay. **(E-**
1051 **F)** A heatmap **(E)** and a peri-event plot **(F)** of calcium transients of LPB^{CCK} neurons in
1052 a mouse evoked by rat exposure (5 trials) (gray dotted line, onset of approach to the live
1053 rat; dark dotted line, onset of flight. **(G)** Average calcium transients of the tested animals
1054 during the rat exposure assay (n = 5 mice). Shaded areas around means indicate error
1055 bars. **(H)** Schematic paradigm of looming stimulus in a nest-containing open field
1056 apparatus. **(I-J)** A heatmap presentation **(I)** and a peri-event plot **(J)** of calcium
1057 transients of LPB^{CCK} neurons in a mouse upon looming stimulus (5 trials). **(K)** Average
1058 calcium transients of the tested animals during the looming assay (n = 5 mice). **(L-M)**
1059 Long session calcium recordings of LPB^{CCK} neurons during rat exposure **(L)** or looming
1060 tests **(M)**. **(N-O)** Correlation analyses between the elevation of calcium transients and
1061 the onset of flight during rat exposure **(N)** or looming tests **(O)**. **(P)** Comparison of
1062 calcium signals LPB^{CCK} neurons evoked by different stimuli. **(Q-R)** Plot depicting the
1063 differences of the amplitude **(Q)** or the area under the curve (AUC) **(R)** of calcium

signal changes in response to different stimuli. ΔAUC, AUC stimulus signal- AUC basal signal.

Figure 4. Optogenetic inhibition of LPB^{CCK} neurons suppressed predator-evoked and visual predator cue-evoked innate flight responses. (A) Left, schematic of light stimulation of and patch-clamp recording of GtACR1-expressing CCK neurons in the LPB. Right, example of action potentials evoked by optogenetic inhibition of LPB^{CCK} neurons from using whole cell patch-clamp recording. **(B)** Schematic diagram of optogenetic inhibition of LPB^{CCK} neurons. **(C)** Representative image showing the GtACR1-EYFP expression in the LPB and optical fiber tip locations above the LPB of a CCK-Cre mouse. **(D-E)** Schematic and the timing and behavioral paradigm of rat exposure assay. **(F-H)** Photoinhibition of LPB^{CCK} neurons increased number of entries towards the rat (danger zone), time spent in the danger zone, with unchanged travel distance (EYFP: n = 6 mice, GtACR1: n = 9 mice; for times of entries, p = 0.0456, t = 2.21, df = 13; Unpaired *t* test; for time in the danger zone, p = 0.0153, t = 2.791, df = 13; Unpaired *t* test; for total distance, p = 0.1246, t = 1.642, df = 13; Unpaired *t* test). **(I-J)** Schematic of the looming test apparatus, the timing and behavioral paradigm of looming-evoked flight-to-nest behavioral test. **(K-L)** Photoinhibition of LPB^{CCK} neurons increased the latency towards the nest and reduced the hiding time in the nest. (EYFP: n = 11 mice, GtACR1: n = 7 mice; for latency, p = 0.0153, t = 2.716, df = 16; Unpaired *t* test; Mann-Whitney test; for time in the nest, p = 0.0201, t = 2.582, df = 16; Unpaired *t* test).

1087 **Figure 5. Photostimulation of the LPB^{CCK}-PVN pathway induces defensive-like**
1088 **flight-to-nest behavior. (A)** Schematic diagram of optogenetic activation of LPB^{CCK}-
1089 PVN pathway. **(B-C)** A representative image showing the ChR2-EYFP expression in
1090 the LPB **(B)** and the optical fiber tip locations in the PVN **(C)** of a CCK-Cre mouse.
1091 **(D)** Schematic of the timing and behavioral paradigm with optical activation of
1092 LPB^{CCK}-PVN pathway. **(E)** Schematic of the experimental apparatus with a nest in the
1093 corner. **(F-H)** Optogenetic activation of the LPB^{CCK}-PVN pathway shortened the
1094 latency but increased the speed of animals towards the nest, with increased hiding time
1095 in the nest (EYFP: n = 7 mice, ChR2: n = 7 mice; for latency, p = 0.0012, U = 0; Mann-
1096 Whitney test; for speed, p = 0.0013, t = 4.163, df = 12; unpaired *t* test; for time in the
1097 nest, p = 0.0006, U = 0; Mann-Whitney test). **(I-J)** C-fos staining in the PVN **(I)** and
1098 quantification of c-fos positive cells in the PVN **(J)**. Scale bar: 100 μm. (EYFP: n = 3
1099 mice, ChR2: n = 3 mice; p = 0.0033, t = 6.253, df = 4; unpaired *t* test). **(K)** Mean heart
1100 rate analyses in EYFP and ChR2 groups (EYFP: n = 7 mice, ChR2: n = 7 mice; p =
1101 0.0002, t = 5.249, df = 12; unpaired *t* test). **(L)** Example image of computer-detected
1102 pupil size before and during photoactivation of LPB^{CCK} neurons. **(M)** Relative pupil
1103 size of animals (during/before photostimulation of LPB^{CCK} neurons) (EYFP: n = 6 mice,
1104 ChR2: n = 6 mice; p = 0.0022, U = 0; Mann-Whitney test). **(N)** Plasma corticosterone
1105 levels in EYFP and ChR2 groups. (EYFP: n = 5 mice, ChR2: n = 5 mice; P = 0.0079,
1106 U = 0; Mann-Whitney test).
1107
1108 **Figure 6. PVN is involved in the defensive-like flight-to-nest behavior evoked by**

LPB^{CCK} neurons. (A) Schematic of experimental setup. **(B)** Left, representative image showing the ChR2-EYFP expression in the LPB of a CCK-Cre mouse. Scale bar, 100 μm. Right, representative image showing the hM4Di-mCherry expression in the PVN and optic fiber placement in the PVN from a ChR2-EYFP expressing mouse. **(C-E)** Chemogenetic inhibition of PVN neurons before optical activation of LPB^{CCK}-PVN terminals increased latency and reduced the speed of animals towards the nest, with reduced hiding time in the nest (saline: n = 7 mice, CNO: n = 7 mice; for latency, p = 0.0088, t = 3.122, df = 12; unpaired *t* test; for speed, p<0.0001, t = 5.736, df = 12; unpaired *t* test; for time in the nest, p = 0.0032, t = 3.665, df = 12; unpaired *t* test). **(F)** Optogenetic activation of LPB^{CCK} -PVN terminals with a cannula implanted in the PVN for aCSF, CNQX+AP5, or Devazepide + L-365 260 delivery. Scale bar, 100 μm. **(G)** Representative image showing the ChR2-EYFP expression in the LPB of a CCK-Cre mouse. Scale bar, 100 μm. **(H)** Representative image showing the cannula placement in the PVN from a ChR2-EYFP expressing CCK-Cre mouse. Scale bar, 100 μm. **(I-K)** Microinjection of the glutamate receptor antagonists (CNQX + AP5), rather than CCK receptor antagonists (Devazepide + L-365260), into the PVN increased the latency to the nest and reduced the hiding time in the nest (ACSF: n = 6 mice, CNQX + AP5: n = 6 mice, Devazepide + L-365260: n = 5 mice; for latency, F(2,14)=7.658, p=0.057; One-way ANOVA; for speed, F(2,14) = 11.49, p = 0.0011; for time in the nest, One-way ANOVA; F(2,14) = 16.44, p = 0.0002; One-way ANOVA). **(L)** Schematic diagram of optogenetic activation of PVN^{Vglut2} neurons. **(M)** Representative image showing the ChR2-EYFP expression and optical fiber tip locations in the PVN of a Vglut2-Cre

1131 mouse. Scale bar, 100 μm. **(N-P)** Optogenetic activation of PVN^{Vglut2} neurons reduced
1132 the latency, increased the speed of animals towards a nest and the time in the nest.
1133 (EYFP: n = 6 mice, ChR2: n = 6 mice; for latency, p = 0.0065, U = 2; Mann-Whitney
1134 test; for speed, p = 0.0221, t = 2.705, df = 10; unpaired *t* test; for time in the nest, p =
1135 0.022, U = 0; Mann-Whitney test). **(Q)** Graphical summary showing the LPB^{CCK}-PVN
1136 pathway in mediating defensive behaviors.

1137 **Supplementary figure legends**

1138 **Figure 1-figure supplement 1. Anterograde mapping of LPB^{CCK} neurons. (A-I)**
1139 Representative images showing the projections from LPB^{CCK} neurons in the median
1140 preoptic nucleus (MnPO), lateral preoptic area (LPO), paraventricular thalamic nucleus
1141 (PVT), ventromedial hypothalamic nucleus (VMH), ventral posteromedial thalamic
1142 nucleus (VPM), lateral posterior thalamic nucleus, mediorostral part (LPMR),
1143 parasubthalamic nucleus (PSTh), periaqueductal gray (PAG), deep gray layer of the
1144 superior colliculus (DpG）(n = 3 mice; green, GFP; red, mrubby; blue, DAPI). Scale
1145 bar, 100 μm; n = 3 mice.

1146

1147 **Figure 1-figure supplement 2. Distribution and identification of CCK neurons in**
1148 **the LPB. (A)** Schematic of mice crossing to generate the CCK-ires-Cre::Ai14 mice. **(B)**
1149 Representative coronal section images illustrating the expression of CCK-tdT in the
1150 LPB; scale bar, 100 μm. **(C)** Quantification of CCK-tdT cells across the rostral-to-
1151 caudal extent of the LPB; n = 3 mice. **(D)** Representative images showing co-labeling
1152 (arrowheads) of Vglut2-positive (Green) and CCK-tdT expressing cells in the LPB.
1153 Rightmost panel, magnification of the box-shaped area in the left panel (white dashed
1154 lines). Blue, DAPI staining. Scale bar, 100 μm. **(E)** Example images showing Vgat-
1155 positive (Green) and CCK-tdT-expressing cells in the LPB. Rightmost panel,
1156 magnification of the boxed area in the left panel. Blue, DAPI staining. Scale bar, 100
1157 μm. **(F)** Representative image from a CCK-ires-Cre::Ai14 mouse in the LPB region
1158 stained with antibodies against CGRP. Rightmost panels, magnification of the boxed

areas in the left panels. Blue, DAPI staining. Scale bar, 100 μm. **(G)** Percentage of CCK^+ neurons that co-localized with markers; n = 4 mice.

Figure 2-figure supplement 3. Photostimulation of LPB^{CCK} neurons induces anxiety-like behaviors. (A) Schematic of behavioral test protocol. OFT, open field test; EPM, elevated plus maze test. **(B)** Experimental apparatus: Open field. **(C)** Example movement traces of a control (AAV2/9-EF1a-DIO-EYFP, left) and an experimental mouse (AAV2/9-EF1a-DIO-ChR2-EYFP, right) in the OFT. **(D-F)** Quantification of the total distance moved, time spent in the center and total number of center entries in the OFT before (Pre) and after (Post) photostimulation of LPB^{CCK} neurons in CCK-Cre mice (EYFP and ChR2, n = 7 mice; for total distance, Pre- light vs. Post-light EYFP $p > 0.9999$, Post-light EYFP vs. ChR2, $p = 0.2236$, Pre-light vs. Post-light ChR2, $p = 0.9026$; two-way ANOVA, Bonferroni's multiple comparisons test; for center time, Pre-light vs. Post-light EYFP, $p > 0.9999$, Post-light EYFP vs. Post-light ChR2 $^{**}p < 0.01$ $p = 0.005$, Pre-light ChR2 vs. Post-light ChR2 $^{**}p < 0.01$ $p = 0.005$; two-way ANOVA, Bonferroni's multiple comparisons test; for center entries, Pre-light EYFP vs. Post-light EYFP ns $p > 0.9999$, Post-light EYFP vs. Post-light ChR2 $^{***}p < 0.0005$ $p = 0.0004$, Pre-light ChR2 vs. Post-light ChR2 $^{**}p < 0.01$ $p = 0.0042$; two-way ANOVA, Bonferroni's multiple comparisons test). **(G)** Experimental apparatus: Elevated plus maze. **(H)** Example traces of a control group mouse (AAV2/9-EF1a-DIO-EYFP, left) and an experimental group mouse (AAV2/9-EF1a-DIO-EYFP, right) in the elevated plus maze. **(I-J)** Quantification of the open arm time and entries in the elevated plus

1181 maze tests before (Pre) and after (Post) photostimulation of LPB^{CCK} neurons in CCK-
1182 Cre mice. (EYFP: n = 7 mice, ChR2: n = 7 mice; for open arm time, Pre-light EYFP vs.
1183 Post-light EYFP ns $p > 0.9999$, Post-light EYFP vs. Post-light ChR2 **$p < 0.01$ $p =$
1184 0.0053, Pre-light ChR2 vs. Post-light ChR2 ***$p<0.0005$ $p = 0.0005$; two-way
1185 ANOVA, Bonferroni's multiple comparisons test; for open arm entries, Pre-light EYFP
1186 vs. Post-light EYFP ns $p > 0.9999$, Post-light EYFP vs. Post-light ChR2 **$p < 0.01$ p
1187 $= 0.0159$, Pre-light ChR2 vs. Post-light ChR2 ****$p < 0.0001$; two-way ANOVA,
1188 Bonferroni's multiple comparisons test).
1189
1190 **Figure 3-figure supplement 4. LPB^{CCK} neurons respond to threat stimuli.** (A) A
1191 schematic of the heat assay. (B) Representative trial-by-trial heatmap presentation of
1192 calcium transients evoked by heat exposure in 5 trials from one mouse. (C)
1193 Representative peri-event plot of the 1 trial of calcium transients. (D) Average calcium
1194 transients for the 5 trials from one mouse. **(E)** Toy rat assay schematic. Mice were
1195 placed in the presence of a toy rat. **(F)** Representative trial-by-trial heatmap presentation
1196 of calcium transients evoked by toy rat exposure in 1 trial from one mouse. **(G)**
1197 Representative peri-event plot of the 5 trials of calcium transients. **(H)** Average calcium
1198 transients for the entire test group. **(I)** TMT odor exposure schematic. **(J)**
1199 Representative trial-by-trial heatmap presentation of calcium transients evoked by rat
1200 exposure in 1 trial from one mouse. **(K)** Representative peri-event plot of the 5 trials of
1201 calcium transients. **(L)** Average calcium transients for the entire test group.
1202

Figure 6-supplymentary 5. Stimulation of LPB^{CCK}-PVN pathway activates PVN^{CRH} neurons, but activation of PVN^{CRH} neurons does not trigger flight-to-nest behavior. (A-B) Representative histological images showing CCKaR and CCKbR in the PVN. **(C)** C-fos expression and colocalization (arrows) with CRH in the PVN with blue light activation of LPB-originating ChR2-EYFP expressing terminals in the PVN. Scale bar: 100 μm. **(D)** Quantification for the percentage of activated CRH neurons in the PVN following blue light activation. (EYFP: n = 3 mice, ChR2: n = 3 mice; p = 0.0066, t = 5.187, df = 4; unpaired *t* test). **(E-F)** Left: C-fos expression and colocalization (arrows) with OXT in the PVN with blue light activation of LPB-originating ChR2-EYFP expressing terminals in the PVN. Scale bar: 100 μm. Right: C-fos expression and colocalization (arrows) with AVP in the PVN with blue light activation of LPB-originating ChR2-EYFP expressing terminals in the PVN. Scale bar: 100 μm. **(G)** Schematic diagram of optogenetic activation of PVN^{CRH} neurons. **(H)** Representative image showing the ChR2-EYFP expression and optical fiber tip locations in the PVN of a CRH-Cre mouse. Scale bar, 100 μm. **(I-K)** Optogenetic activation of PVN^{CRH} neurons did not induce flight-to-nest behavior. Compared with control group, ChR2 group showed no changes in latency, speed back into the nest and percentage of hiding time spent in the nest (EYFP: n = 5 mice, ChR2: n = 6 mice; for latency, p = 0.6664, t = 0.4456, df = 9; unpaired t test; for speed, p = 0.0221, t = 2.705, df = 10; unpaired t test; for time in the nest, p = 0.2088, t = 1.367, df = 8; unpaired *t* test).

Figure 1

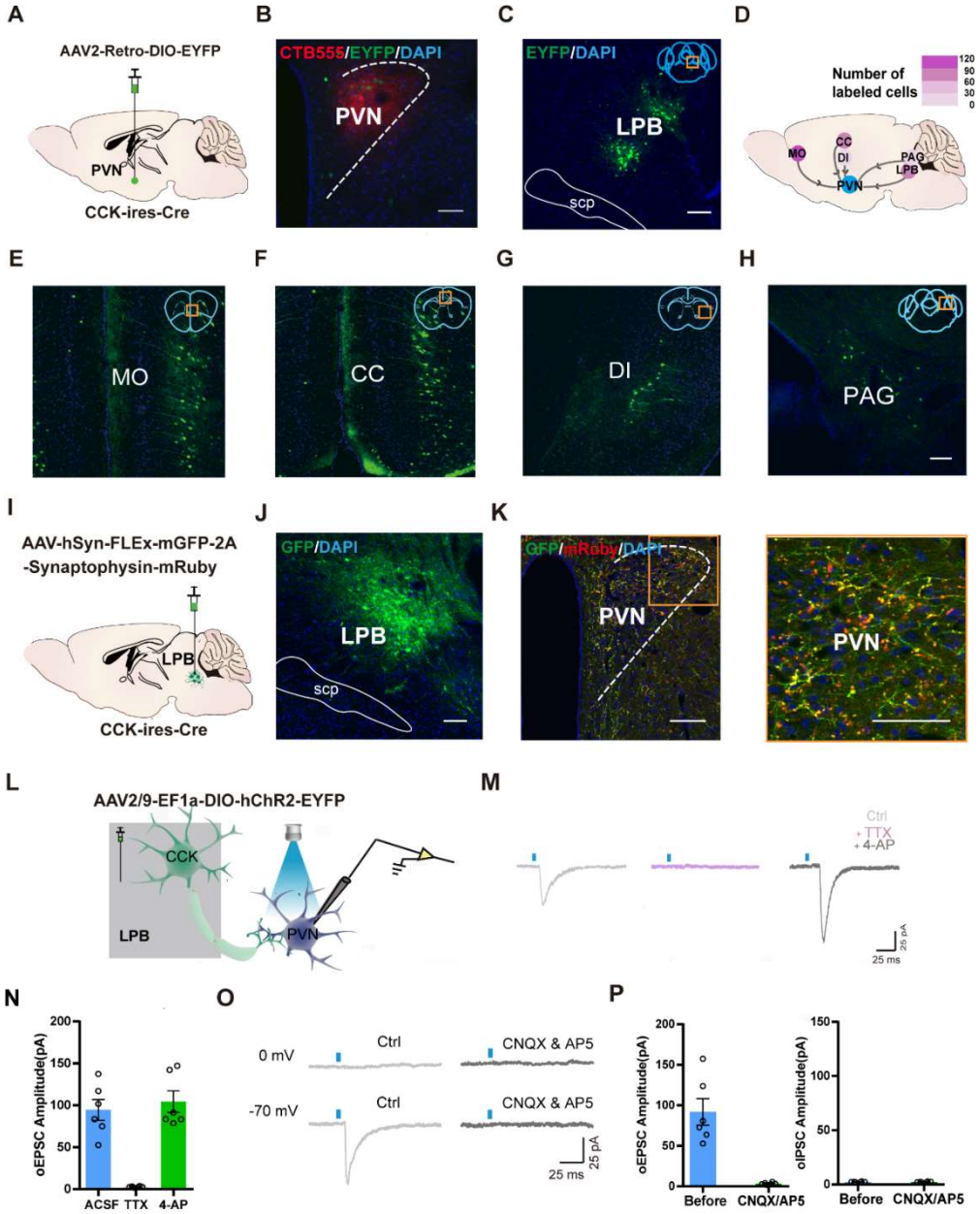
A
AAV2-Retro-DIO-EYFP
PVN
CCK-ires-Cre
B
CTB555/EYFP/DAPI
PVN
C
EYFP/DAPI
LPB
scp
D
Number of labeled cells
120
90
60
30
0
MO
CC
DI
PAG
LPB
PVN
E
MO
F
CC
G
DI
H
PAG
I
AAV-hSyn-FLEx-mGFP-2A -Synaptophysin-mRuby
LPB
CCK-ires-Cre
J
GFP/DAPI
LPB
scp
K
GFP/mRuby/DAPI
PVN
PVN
L
AAV2/9-EF1a-DIO-hChR2-EYFP
CCK
LPB
PVN
M
Ctrl
+TTX
+4-AP
25 pA
25 ms
N
oEPSC Amplitude(pA)
200
150
100
50
0
ACSF
TTX
4-AP
O
0 mV
Ctrl
CNQX & AP5
-70 mV
Ctrl
CNQX & AP5
25 pA
25 ms
P
oEPSC Amplitude(pA)
Before
CNQX/AP5
oIPSC Amplitude(pA)
Before
CNQX/AP5

Figure 2

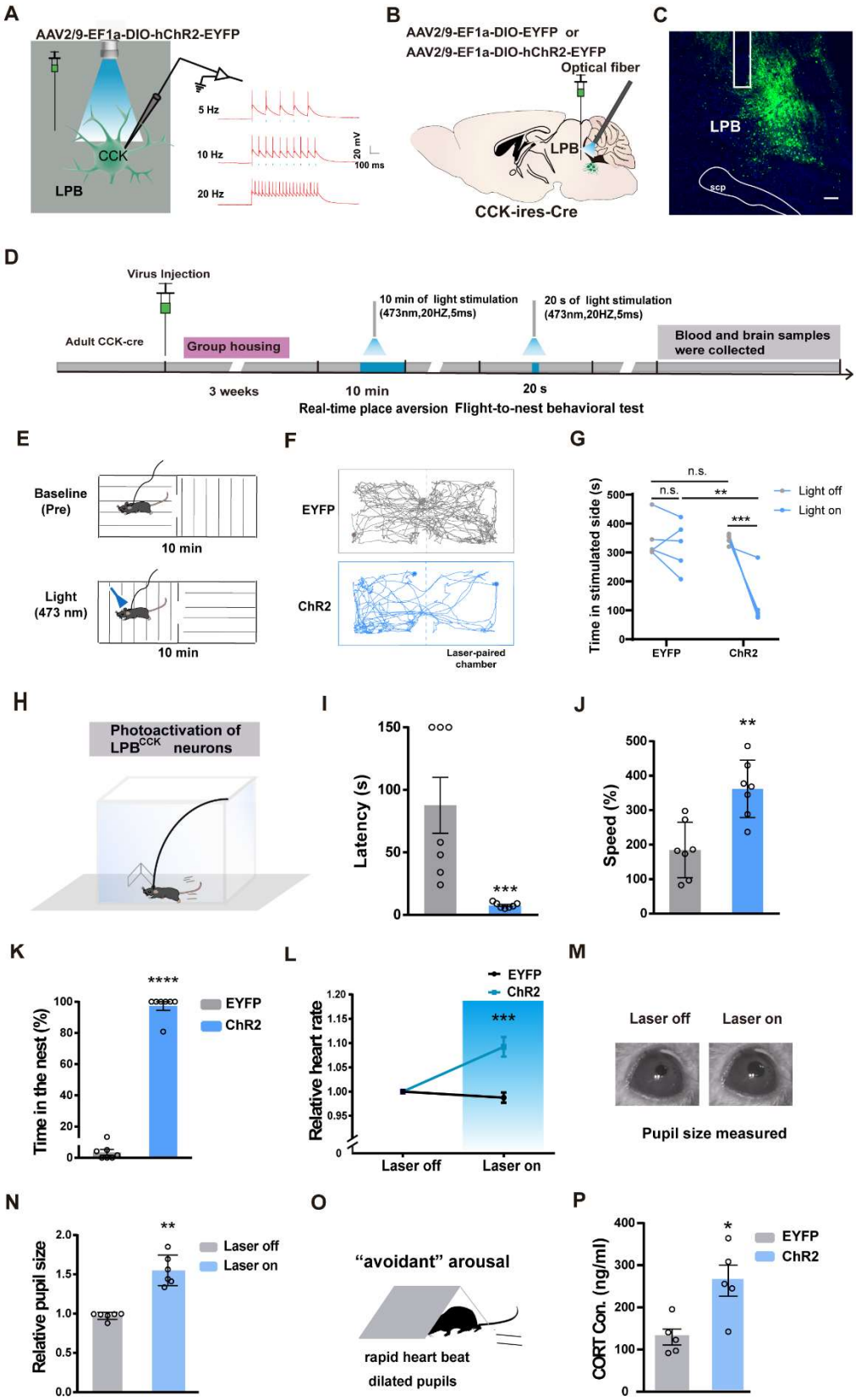
A
AAV2/9-EF1a-DIO-hChR2-EYFP
CCK
LPB
5 Hz
10 Hz
20 Hz
20 mV
100 ms
B
AAV2/9-EF1a-DIO-EYFP or
AAV2/9-EF1a-DIO-hChR2-EYFP
Optical fiber
LPB
CCK-ires-Cre
C
LPB
scp
D
Virus Injection
Adult CCK-cre
Group housing
10 min of light stimulation (473nm,20HZ,5ms)
20 s of light stimulation (473nm,20HZ,5ms)
Blood and brain samples were collected
3 weeks
10 min
20 s
Real-time place aversion
Flight-to-nest behavioral test
E
Baseline (Pre)
10 min
Light (473 nm)
10 min
F
EYFP
ChR2
Laser-paired chamber
G
Time in stimulated side (s)
n.s.
n.s.
**
***
Light off
Light on
EYFP
ChR2
H
Photoactivation of LPB^CCK neurons
I
Latency (s)
***
J
Speed (%)
**
K
Time in the nest (%)
****
EYFP
ChR2
L
Relative heart rate
EYFP
ChR2
***
Laser off
Laser on
M
Laser off
Laser on
Pupil size measured
N
Relative pupil size
**
Laser off
Laser on
O
"avoidant" arousal
rapid heart beat
dilated pupils
P
CORT Con. (ng/ml)
*
EYFP
ChR2

Figure 3

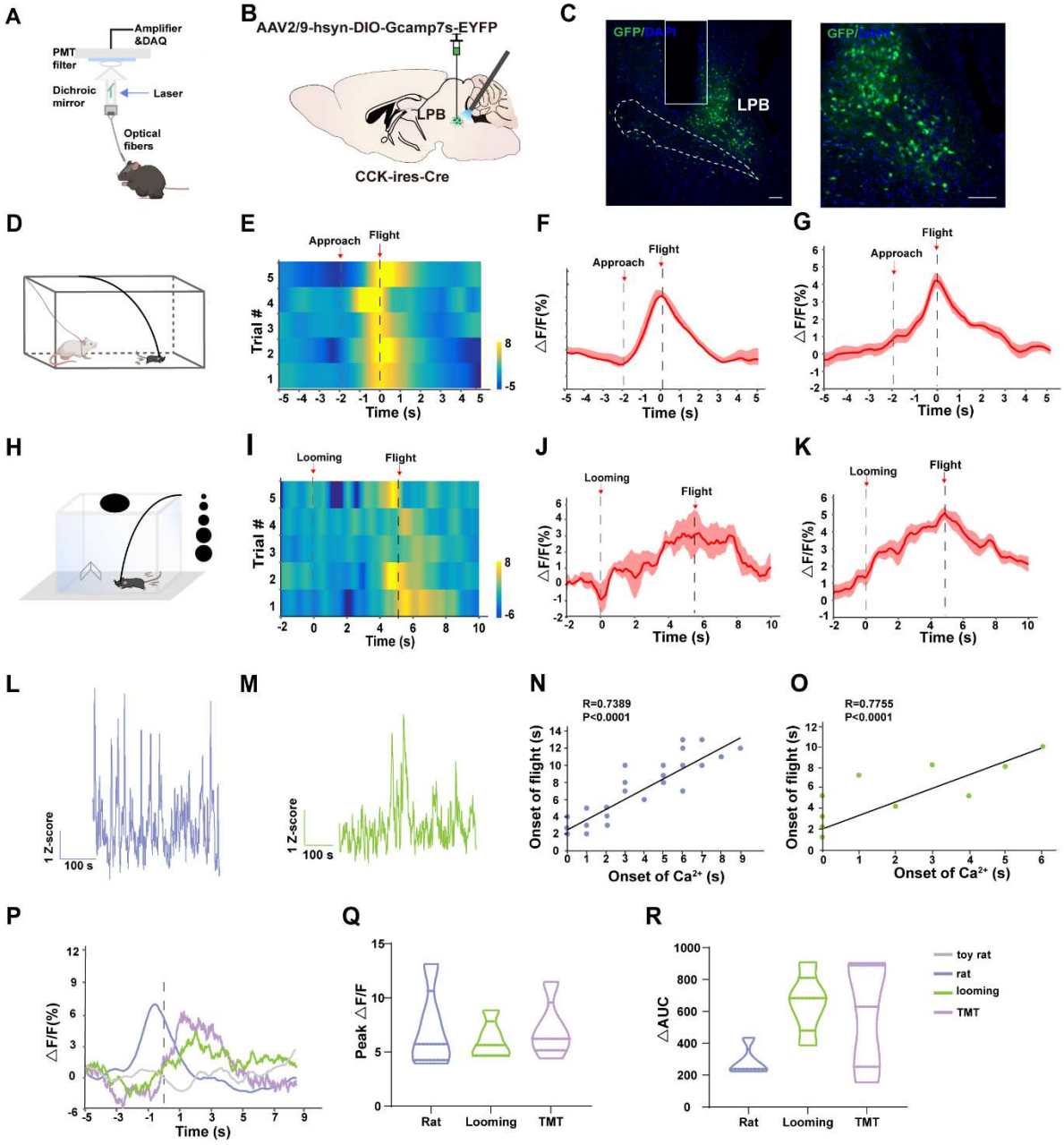
A
Amplifier &DAQ
PMT filter
Dichroic mirror
Laser
Optical fibers
B
AAV2/9-hsyn-DIO-Gcamp7s-EYFP
LPB
CCK-ires-Cre
C
GFP/DAPI
LPB
D
E
Approach
Flight
Trial #
Time (s)
F
Approach
Flight
△F/F(%)
Time (s)
G
Approach
Flight
△F/F(%)
Time (s)
H
I
Looming
Flight
Trial #
Time (s)
J
Looming
Flight
△F/F(%)
Time (s)
K
Looming
Flight
△F/F(%)
Time (s)
L
1 Z-score
100 s
M
1 Z-score
100 s
N
R=0.7389
P<0.0001
Onset of flight (s)
Onset of Ca²⁺ (s)
O
R=0.7755
P<0.0001
Onset of flight (s)
Onset of Ca²⁺ (s)
P
△F/F(%)
Time (s)
Q
Peak △F/F
Rat
Looming
TMT
R
△AUC
Rat
Looming
TMT
toy rat
rat
looming
TMT

1236 **Figure 4**

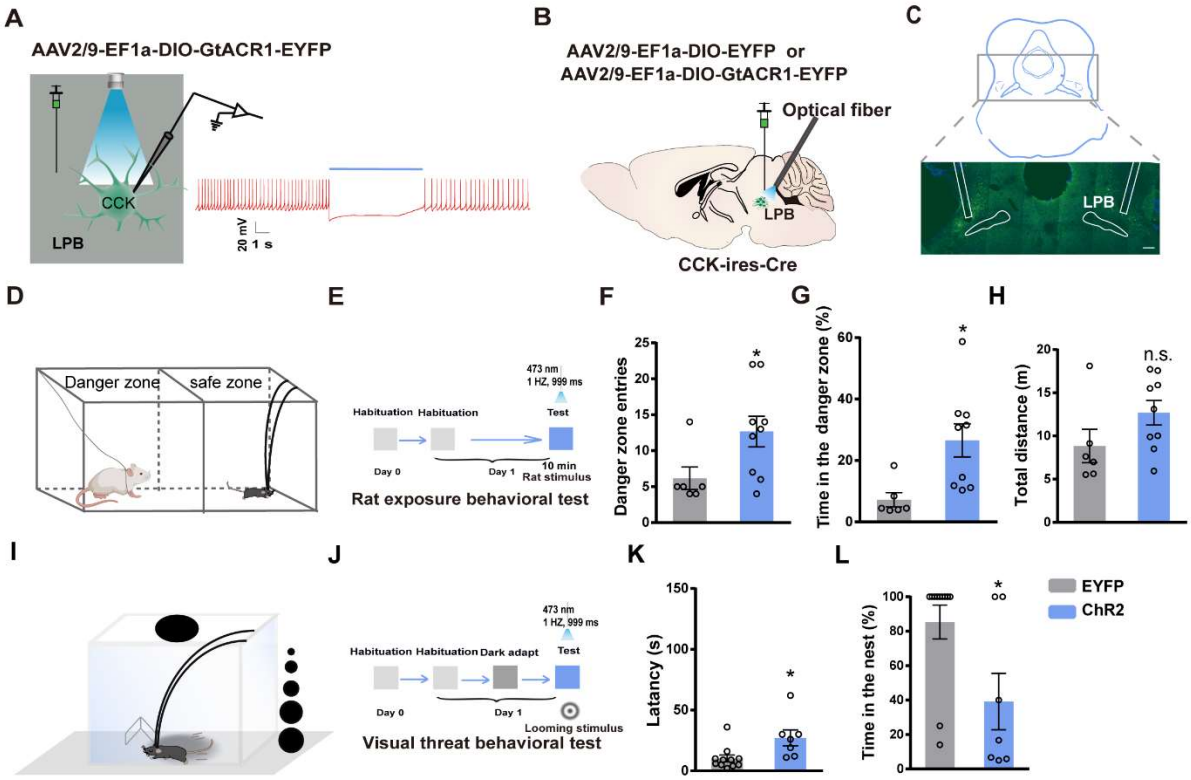

1237

Figure 5

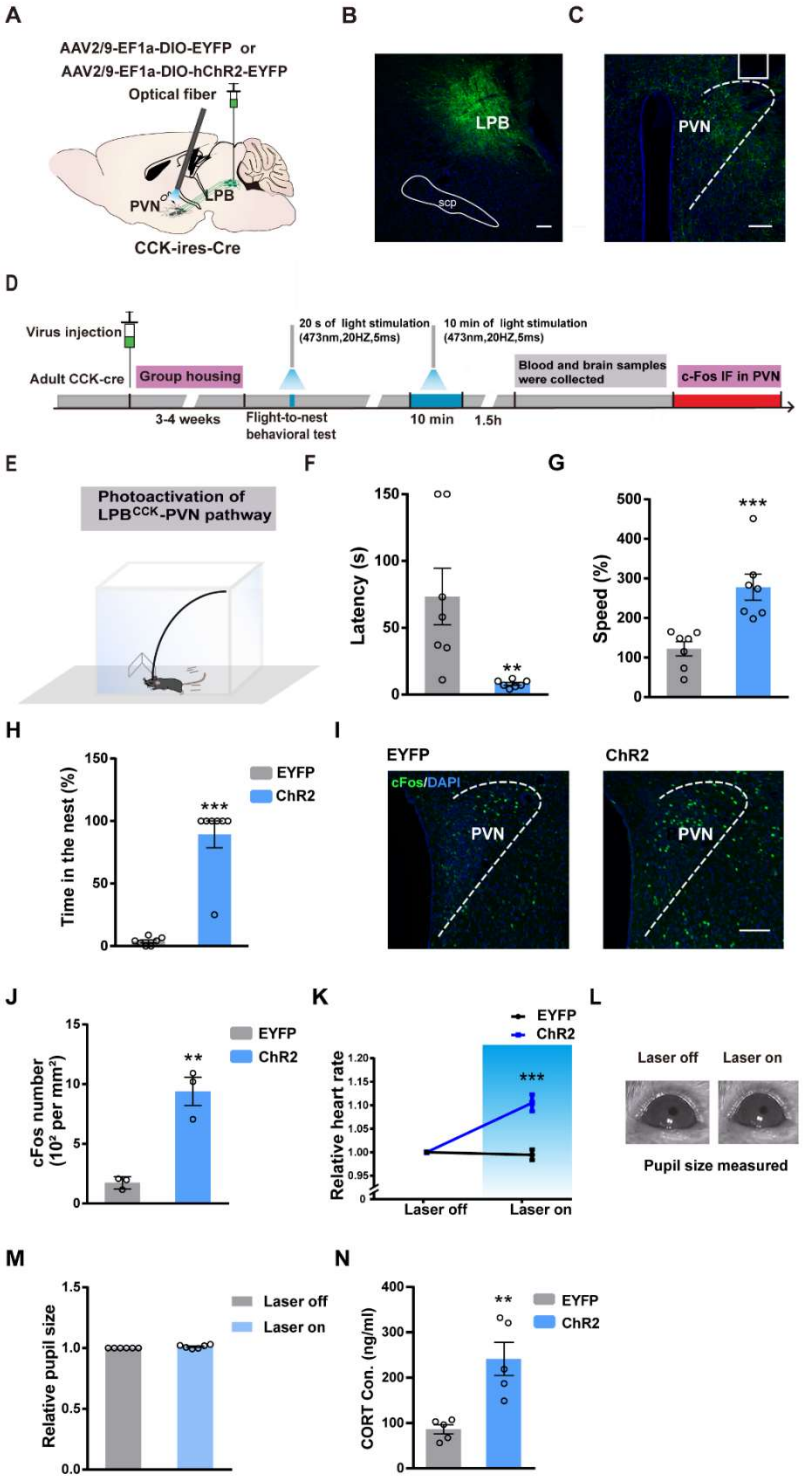
A
AAV2/9-EF1a-DIO-EYFP or
AAV2/9-EF1a-DIO-hChR2-EYFP
Optical fiber
PVN
LPB
CCK-ires-Cre
B
LPB
scp
C
PVN
D
Virus injection
Adult CCK-cre
Group housing
20 s of light stimulation (473nm,20HZ,5ms)
10 min of light stimulation (473nm,20HZ,5ms)
Blood and brain samples were collected
c-Fos IF in PVN
3-4 weeks
Flight-to-nest behavioral test
10 min
1.5h
E
Photoactivation of LPB^{CCK}-PVN pathway
F
Latency (s)
G
Speed (%)
H
Time in the nest (%)
EYFP
ChR2
I
EYFP
ChR2
cFos/DAPI
PVN
J
cFos number (10^2 per mm^2)
K
Relative heart rate
Laser off
Laser on
L
Laser off
Laser on
Pupil size measured
M
Relative pupil size
Laser off
Laser on
N
CORT Con. (ng/ml)

Figure 6

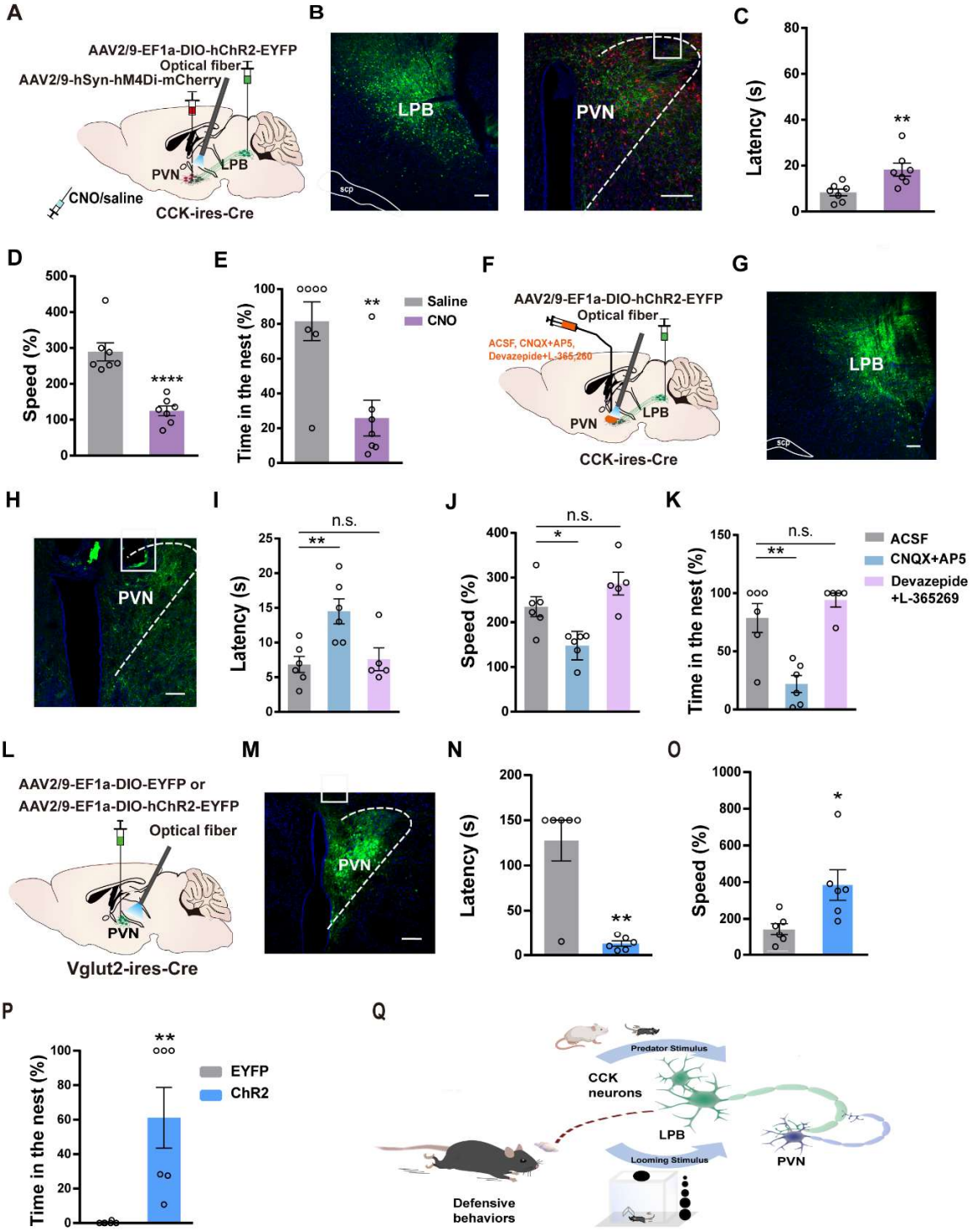
A
AAV2/9-EF1a-DIO-hChR2-EYFP
Optical fiber
AAV2/9-hSyn-hM4Di-mCherry
PVN
LPB
CNO/saline
CCK-ires-Cre
B
LPB
PVN
C
Latency (s)
D
Speed (%)
E
Time in the nest (%)
Saline
CNO
F
AAV2/9-EF1a-DIO-hChR2-EYFP
Optical fiber
ACSF, CNQX+AP5,
Devazepide+L-365,260
PVN
LPB
CCK-ires-Cre
G
LPB
H
PVN
I
Latency (s)
n.s.
J
Speed (%)
n.s.
K
Time in the nest (%)
n.s.
ACSF
CNQX+AP5
Devazepide
+L-365269
L
AAV2/9-EF1a-DIO-EYFP or
AAV2/9-EF1a-DIO-hChR2-EYFP
Optical fiber
PVN
Vglut2-ires-Cre
M
PVN
N
Latency (s)
O
Speed (%)
P
Time in the nest (%)
EYFP
ChR2
Q
Predator Stimulus
CCK
neurons
LPB
Looming Stimulus
PVN
Defensive
behaviors

1244 **Figure1-supplymentary1**

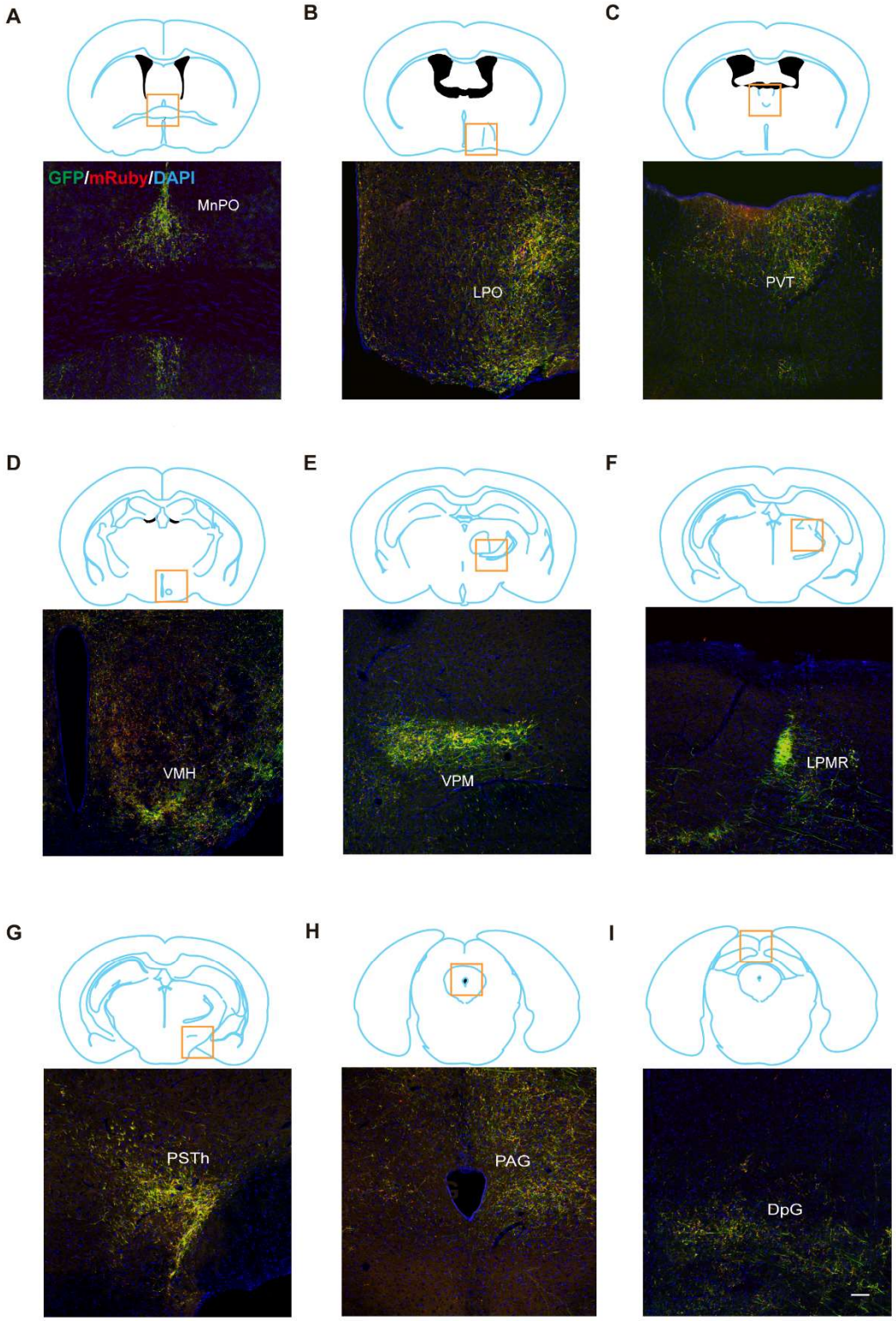

1245

Figure1-supplymentary2

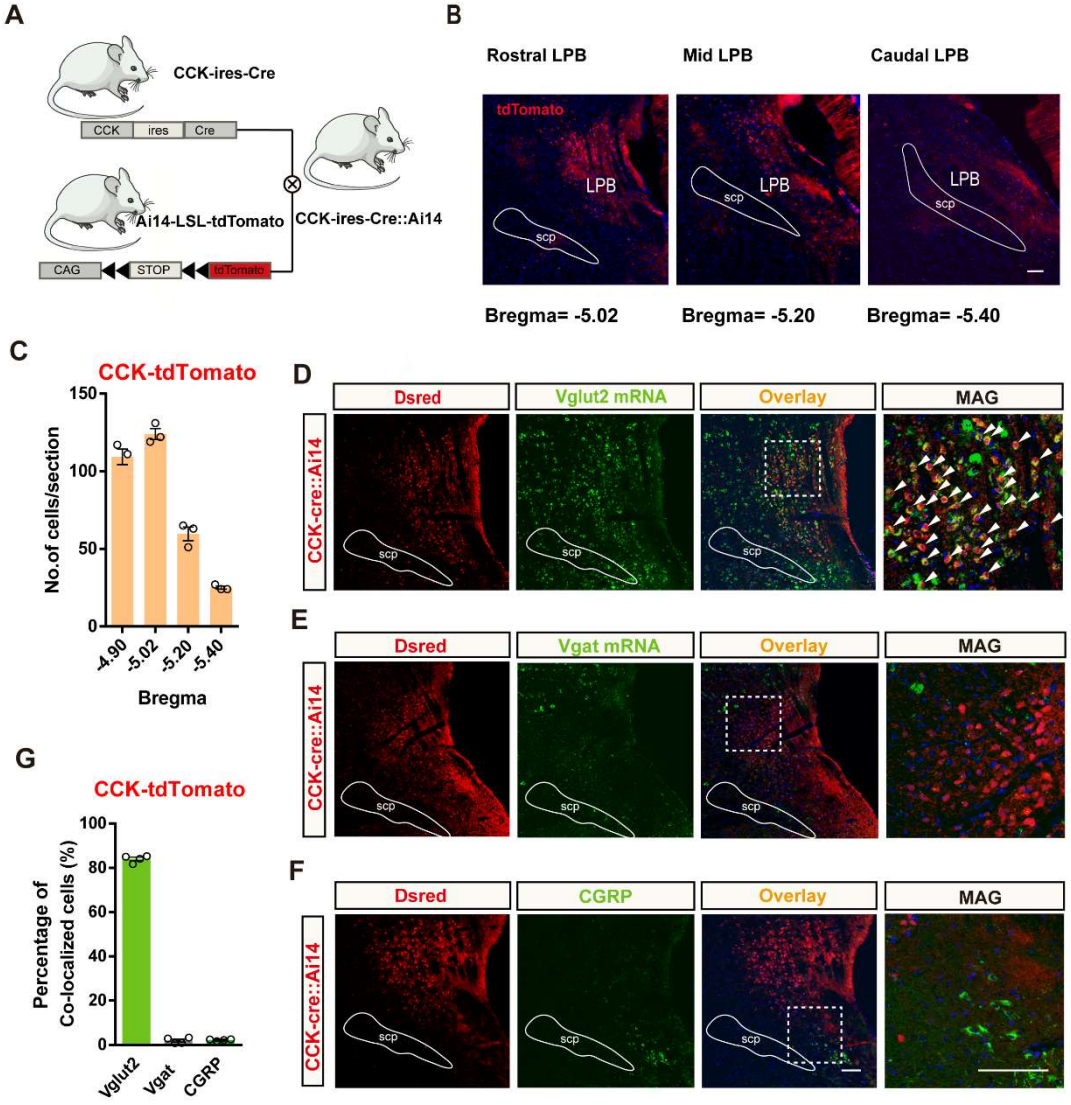

Figure2-supplymentary3

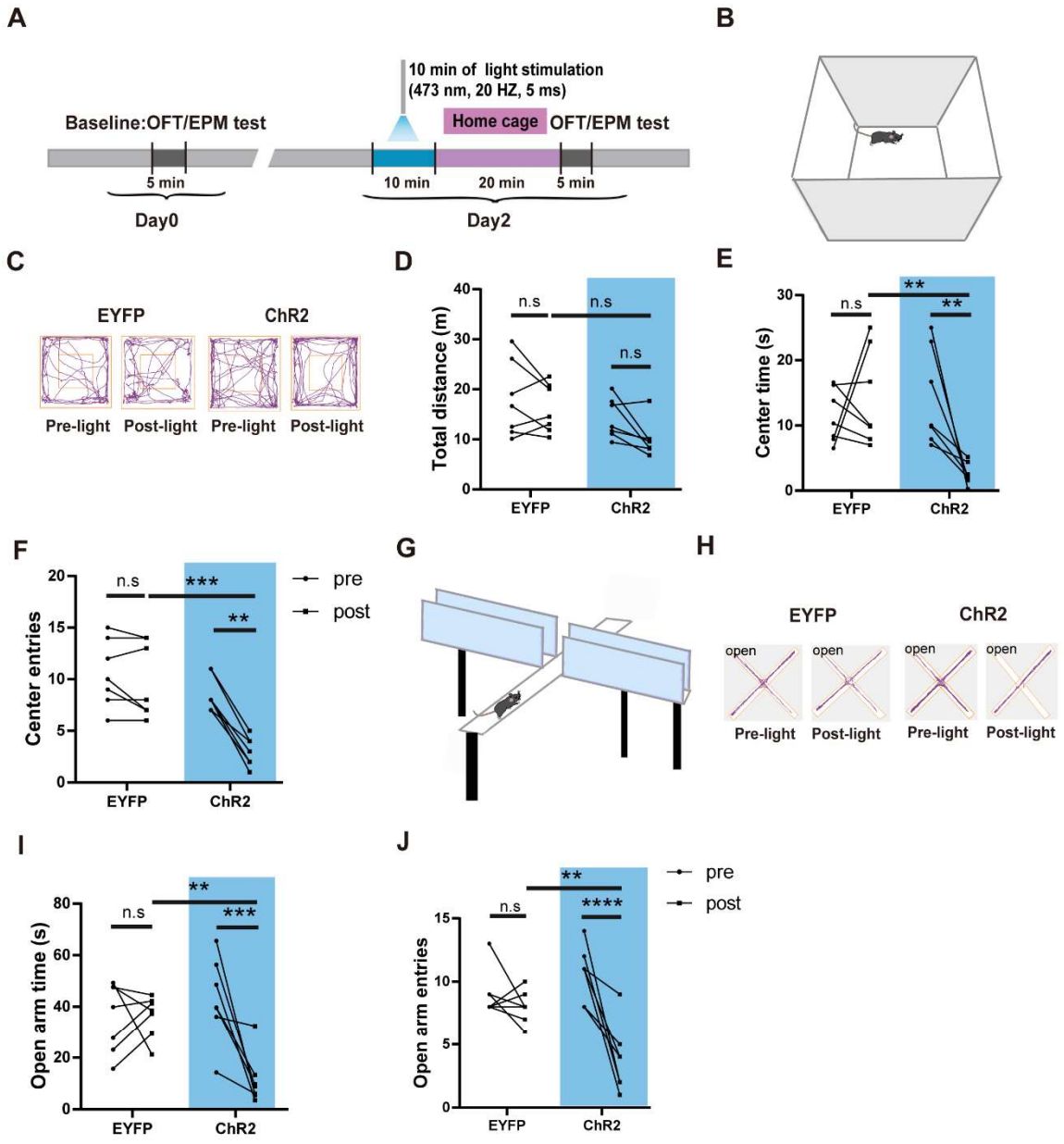

Figure3-supplymentary4

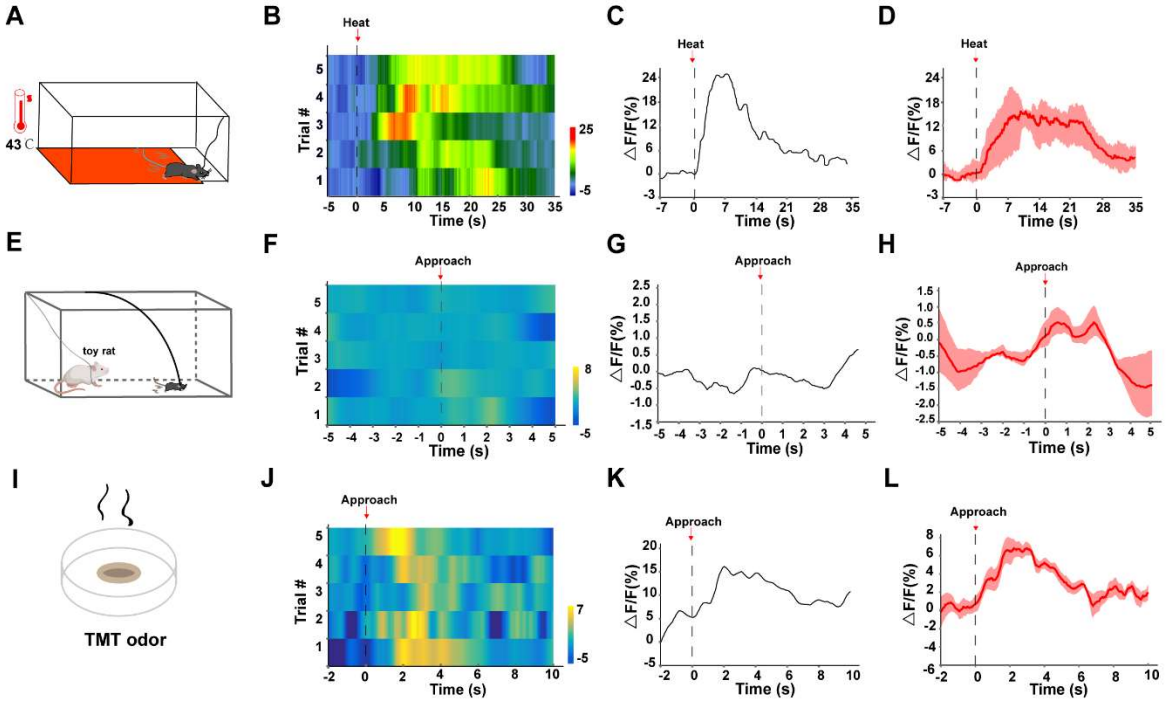
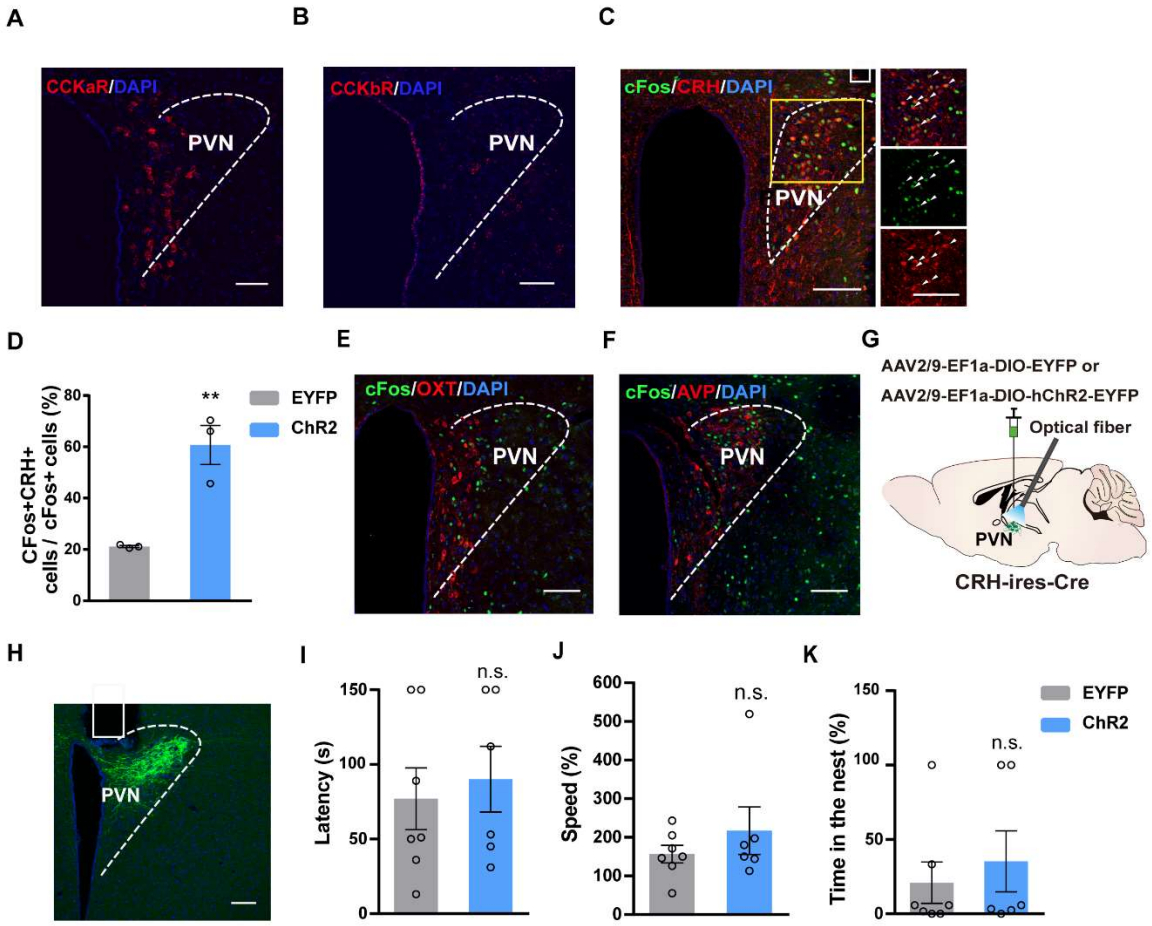
Figure6-supplymentary5